LUND UNIVERSITY

Extensive Gamma-ray Spectroscopy of Band Structures in 62Zn

Gellanki, Jnaneswari; Rudolph, Dirk; Ragnarsson, Ingemar; Andersson, Lise-Lotte; Andreoiu, Corina; Carpenter, M. P.; Ekman, Jörgen; Fahlander, Claes; Johansson, Emma; Kardan, A.; Reviol, W.; Sarantites, D. G.; Seweryniak, D.; Svensson, C. E.; Waddington, J. C.

Link to publication

LUND UNIVERSITY

PO Box 117
221 00 Lund
+46 46-222 00 00

Extensive γ-ray spectroscopy of band structures in $^{62}_{30}$Zn$_{32}$

J. Gellanki,[1] D. Rudolph,[1] I. Ragnarsson,[2] L.-L. Andersson,[1,*] C. Andreoiu,[1,†] M. P. Carpenter,[3] J. Ekman,[1,‡] C. Fahlander,[1]
E. K. Johansson,[1] A. Kardan,[4] W. Reviol,[5] D. G. Sarantites,[5] D. Seweryniak,[3] C. E. Svensson,[6] and J. C. Waddington[6]

[1]*Department of Physics, Lund University, S-22100 Lund, Sweden*
[2]*Division of Mathematical Physics, LTH, Lund University, S-22100 Lund, Sweden*
[3]*Physics Division, Argonne National Laboratory, Argonne, Illinois 60439, USA*
[4]*Physics Department, Ferdowsi University of Mashhad, Box 91775-1436, Mashhad, Iran*
[5]*Chemistry Department, Washington University, St. Louis, Missouri 63130, USA*
[6]*Department of Physics, University of Guelph, Guelph, Ontario, Canada N1G 2W1*

An experimental study of the ^{62}Zn nucleus has been performed by combining the data sets from four fusion-evaporation reaction experiments. Apart from the previously published data, the present results include ten new rotational band structures and two more superdeformed bands. The Gammasphere Ge-detector array in conjunction with the 4π charged-particle detector array Microball allowed for the detection of γ rays in coincidence with evaporated light particles. The deduced level scheme includes some 260 excited states, which are connected with more than 450 γ-ray transitions. Spins and parities of the excited states have been determined via directional correlations of γ rays emitted from oriented states. The experimental characteristics of the rotational bands are analyzed and compared with results from cranked Nilsson-Strutinsky calculations. The present analysis, combined with available experimental results in the $A \sim 60$ mass region, can be used to improve the current set of Nilsson parameters in the $\mathcal{N} = 3$ and $\mathcal{N} = 4$ oscillator shells.

I. INTRODUCTION

The investigation of high angular momentum states in atomic nuclei has long been a topical question in nuclear structure physics. Here, reliable and comprehensive high-spin studies of neutron-deficient nuclei in the mass $A \sim 60$ region require extra efforts compared to studies of heavier nuclei. Especially, the Doppler correction of the rather high-energy transitions in these nuclei is a severe challenge. With the combination of advanced γ-ray and particle-detector arrays such as Gammasphere [1] and Microball [2] these difficulties can be handled. This resulted in several nuclear structure highlights in $N \sim Z$, $A \sim 60$ nuclei such as, to name but a few, discrete-energy particle decay-out transitions [3–6], quests for isospin $T = 0$ pairing [7,8], record-high rotational frequencies [9], or "complete" high-spin excitations schemes comprising coexisting spherical, deformed, and superdeformed states [10,11].

High-spin collectivity in the $A \sim 60$ mass region is induced by particle-hole excitations across the spherical shell gap at particle number $N = Z = 28$. A limited number of holes in the $1f_{7/2}$ subshell and excitation of one or more nucleons into $1g_{9/2}$ intruder orbitals above the ^{56}Ni closed core give rise to nuclear structure phenomena associated with collective excitations, including superdeformation [10–18], favored and unfavored band termination [19–21], as well as bands with strong magnetic dipole transitions [21–24]. Unlike in other mass regimes, almost all high-spin bands in the mass $A \sim 60$ region are seen to be connected with the low-spin spherical states in the first minimum of the nuclear potential, be it by γ rays or proton- or α-decay lines.

Previously published data on ^{62}Zn includes low- and medium-spin structures, a superdeformed band, and two terminating bands [17,20]. Our most recent study highlighted three superdeformed bands together with one well-deformed band [18]. The present paper may be viewed as the summarizing high-spin spectroscopy study of ^{62}Zn.

Following this Introduction, a brief description of the experiments and analysis tools is provided in Sec. II. The results concerning the different structures of the complex decay scheme are presented in detail in Sec. III. The experimentally observed states are systematically discussed in the framework of the cranked Nilsson-Strutinsky approach in Sec. IV, thereby adding some new information to the previously published results [17,18,20].

II. EXPERIMENTAL DETAILS AND ANALYSIS PROCEDURES

The results presented in this paper originate from the combined statistics of four different experiments carried out at Argonne and Lawrence Berkeley National Laboratories. A brief description is given below. More detailed explanations about the experiments are, for example, provided in Refs. [10,25,26].

Data set 1. One experiment used the fusion-evaporation reaction ^{40}Ca(^{28}Si,$1\alpha2p$)^{62}Zn at a beam energy of 122 MeV. The target had an isotopic enrichment of 99.975% and a thickness of 0.5 mg/cm^2. ^{62}Zn nuclei were populated with $\approx$30% of the total fusion cross section. The experimental

*Present address: Helmholtz-Institut Mainz, D-55099 Mainz, Germany.

†Present address: Department of Chemistry, Simon Fraser University, Burnaby, BC, Canada V5A 1S6.

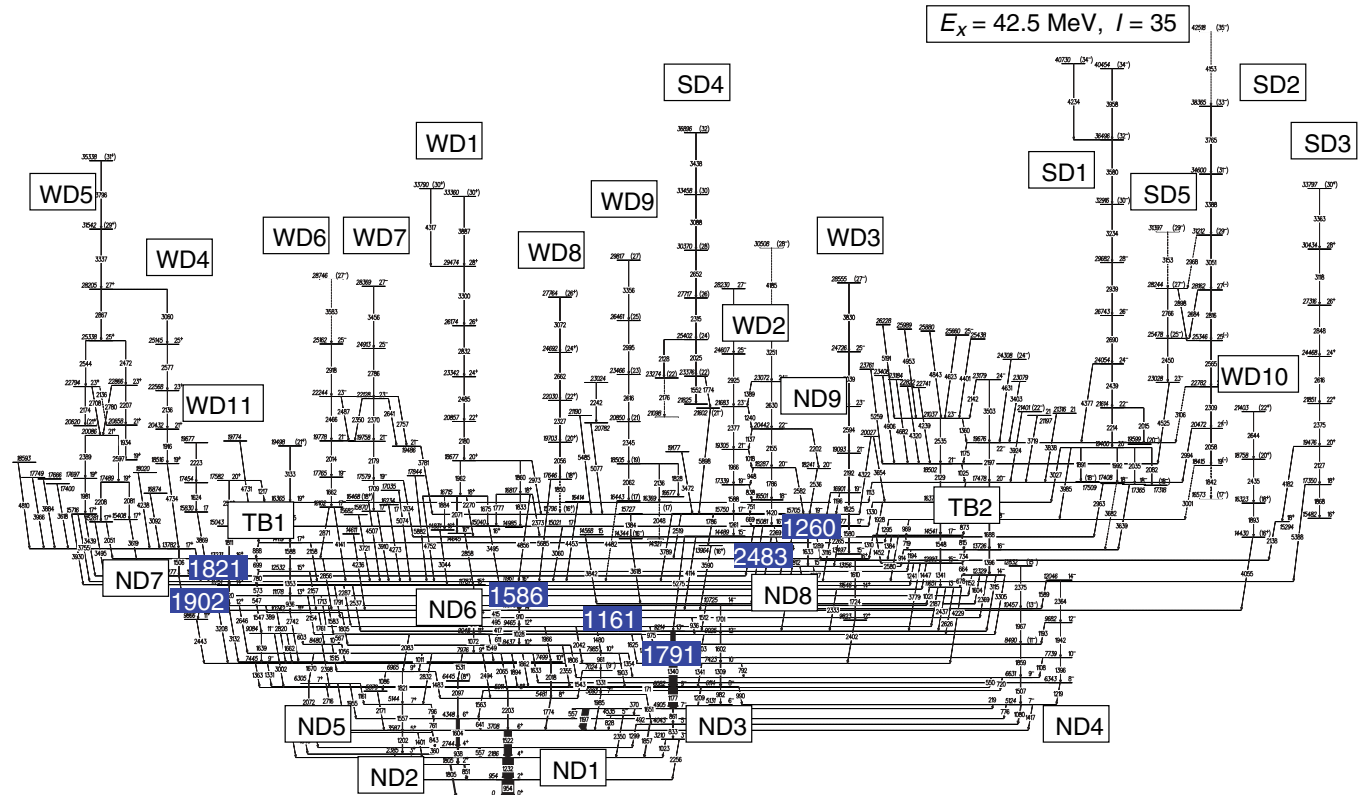‡Present address: Malmö högskola, S-20506 Malmö, Sweden.

FIG. 1. (Color online) Overview of the proposed high-spin level scheme of ^{62}Zn. The structures are labeled according to the descriptions and discussions in the text. Detailed decay schemes of each structure or band are presented in subsequent figures. The transitions marked in blue are significant for the linking of well-deformed and superdeformed bands. See Ref. [29] for a detailed version of the complete excitation scheme of ^{62}Zn.

setup consisted of the Gammasphere array (103 Ge detectors at the time of experiment) in combination with the Microball charged-particle array [2] inside the target chamber. The Heavimet collimators were removed from the Ge-detector modules to provide γ-ray multiplicity and sum-energy measurements [27], as well as additional channel selectivity based on total energy conservation requirements [28]. The statistics from this experiment are denoted as "data set 1." In fact, data set 1 was the main source used to construct the level scheme of ^{62}Zn displayed in Fig. 1 and provided via Ref. [29]. The role of data set 1 is to identify the normally deformed, low- and high-spin rotational and, most importantly, superdeformed bands including their decay-out transitions.

Data set 2. Three Gammasphere experiments have been performed using the fusion-evaporation reaction ^{28}Si(^{36}Ar,2p)^{62}Zn at beam energies of about 140 MeV. Increasingly complex charged-particle detection systems were employed aiming at high-resolution particle-γ coincidence spectroscopy (see, e.g., Refs. [3,11,26] for more details), and arrays of neutron detectors replaced a number of Ge-detector modules at forward angles. In all these experiments, the Heavimet collimators were removed. Hence, by applying specific selection criteria on the data (see below), the combined statistics of these three experiments (called "data set 2") allowed to add the highest-spin states of the superdeformed bands, despite the fact that the relative yield for the production

of ^{62}Zn residues is less than 1% at such high compound nucleus excitation energies.

An event-by-event kinematical reconstruction of the momenta of the recoil nuclei [30] was performed for all four experiments. This allows a more accurate Doppler-shift correction of the γ-ray energies, leading to a significantly improved γ-ray energy resolution. The events were sorted offline into various E_γ projections, E_γ-E_γ matrices, and E_γ-E_γ-E_γ cubes subject to appropriate evaporated-particle conditions, including total γ-ray energy, charged-particle energy, and γ-ray multiplicity conditions for the ^{62}Zn reaction channel.

The analysis employed the RADWARE software package [31] and the spectrum analysis code Tv [32]. Low-intensity or ambiguous transitions were confirmed by specific $\gamma\gamma$ matrices, which were preselected by γ rays originating from a certain rotational band or decay sequence within the complex ^{62}Zn level scheme. For data set 2, a special $\gamma\gamma$ matrix was created, which focused solely on high-lying entry states in ^{62}Zn; here, at least 14 detected γ rays with at least 16.5 MeV total energy and less than 19 MeV particle energy were required, similar to a procedure outlined in Ref. [9]. The level-scheme construction is based on energy and coincidence relationships, intensity balances, and summed-energy considerations.

Assignments of spins and parities of the excited levels were based on the analysis of the 1α2p-gated directional $\gamma\gamma$ correlations of oriented states (DCO ratios). The Ge detectors

of Gammasphere were grouped into three "pseudo" rings called "30," "53," and "83," which correspond to an average angle for the respective set of detectors while accounting for γ-ray emission symmetry with respect to the 90° plane perpendicular to the beam. Matrices for three combinations of the angles were created, namely 30–83, 30–53, and 53–83; for instance, for the latter γ rays detected at 53° were sorted on one axis and those detected at 83° placed on the other axis of the correlation matrix.

The determination of the most discriminating DCO ratios, $R_{\mathrm{DCO}}(30\text{--}83)$, was attempted for all experimentally observed γ-ray transitions, while special emphasis was given to pronounced transitions such as, for example, those linking the deformed or superdeformed rotational bands to the normally deformed low-spin part of the ^{62}Zn level scheme. However, owing to limited statistics, the DCO ratios of some of the γ rays could not be evaluated. The $R_{\mathrm{DCO}}(30\text{--}83)$ values were extracted according to the formula

$$R_{\mathrm{DCO}} = \frac{I(\gamma_1 \text{ at } 30°; \text{ gated with } \gamma_2 \text{ at } 83°)}{I(\gamma_1 \text{ at } 83°; \text{ gated with } \gamma_2 \text{ at } 30°)}, \quad (1)$$

with I denoting the intensities of γ rays in the respective γ-ray coincidence spectra.

The DCO ratios given in Table I were obtained by using known or in the course of the analysis deduced stretched $E2$ transitions as gating transitions (see, for example, Refs. [33–35] for the theoretical background and practical procedures). In this case, for observed stretched $\Delta I = 2$ transitions $R_{\mathrm{DCO}}(30\text{--}83) = 1.0$ is expected. For pure stretched $\Delta I = 1$ transitions, $R_{\mathrm{DCO}}(30\text{--}83) \sim 0.6$. However, $\Delta I = 1$ transitions can show deviations due to quadrupole admixtures, that is, nonzero $\delta(E2/M1)$ mixing ratios. $M2$ and higher multipole orders than quadrupole transitions are neglected owing to their significantly reduced decay probabilities. Nonstretched $\Delta I = 0$ transitions yield typically $R_{\mathrm{DCO}}(30\text{--}83) = 0.9$, that is, numbers similar to stretched $E2$ transitions. Nevertheless, because the γ-ray decay path in nuclei populated via fusion-evaporation reactions follows the yrast line, $\Delta I = 0$ transitions are rare and usually have small relative intensities. Moreover, for complex level schemes such as the one proposed for ^{62}Zn, parallel γ-ray decay branches, often put additional constraints on possible spin and parity assignments to the excited states

An analysis of mixing ratios, $\delta(E2/M1)$, was performed for several $\Delta I = 1$ transitions based on DCO ratios arising from the three different angle combinations. The phase conservation of Rose and Brink [36] is applied, and the procedure follows the one outlined in Ref. [35]. In particular, the alignment coefficients, α_2, were estimated through the relation

$$\alpha_2 = 0.55 + 0.02 \cdot E_x \text{ [MeV]}, \quad \Delta\alpha_2 = \pm 0.05, \quad (2)$$

while limited to a maximum of $\alpha_2 < 0.90$. In case of nonunique solutions of $\delta(E2/M1)$, they are provided in Table I as either two values or estimates or as a range of possible values (cf. Ref. [35]).

III. RESULTS

The level scheme of ^{62}Zn comprises some 260 energy levels and more than 450 γ-ray transitions. An overview of the proposed decay scheme of ^{62}Zn is sketched in Fig. 1. The proposed maximum spin is $I = 35\hbar$ at an excitation energy of $E_x = 42.5$ MeV and rotational frequencies in excess of $\hbar\omega = 2.0$ MeV; numbers are comparable only to ^{58}Ni [9]. Excitation energies, γ-ray energies, relative γ-ray transition yields, angular correlation ratios, and multipolarity assignments are listed in Table I. Notably, the amount of coincidence statistics combined with the resolving power of the experimental setup allowed for unambiguous placements of γ rays with relative yields down to the level of 10^{-4} of the most intense transition.

The figure indicates both the low-spin normally deformed (ND1–ND9) part of the level scheme, the previously published two terminating band structures TB1 and TB2 [20], well-deformed rotational structures (WD2–WD11), as well as the recently highlighted three superdeformed and one well-deformed band structures (SD1–SD3 and WD1) [18]. It includes in addition two more superdeformed band structures (SD4 and SD5). Note that most ND and WD bands are observed to termination and that the notation relates to the theoretical description in Sec. IV A.

In the following, the different sections of the extensive new decay scheme are introduced and described by means of representative γ-ray spectra and R_{DCO} values. All high-spin bands are connected to the low-spin normally deformed states by one or several linking transitions. This allows for either firm, but in some cases only for tentative, spin and parity assignments to the lowest states in the bands. Here, tentative assignments relate also to relative yields of the different bands, that is, the averaged relative intensities of the lowest transitions in each rotational structure before decay out sets in. A typical rule for fusion-evaporation reactions is that the higher the average yield of a structure, the more yrast is the cascade. Tentative spin and parity assignments to the states near the top of the bands are based on their regular rotational behavior.

A. The normally deformed region

Figure 2 provides the low-spin normally deformed (ND) part of the level scheme. In addition to the known low-spin "skeleton" marked ND1, ND2, ND3, and ND6, a rather irregular structure ND5, a bandlike structure ND4, and a relatively intense extension of the medium-spin ^{62}Zn structures ND7, ND8, and ND9 are suggested. The proposed ND parts, that is, Fig. 2 and the associated section of Table I, are consistent with previous studies [37–40], but extend them noticeably. A brief summary of the results is given below, while a more complete analysis can be found in Ref. [41].

The structures ND1 and ND2 mark the well-established positive-parity "backbone" of the level scheme of ^{62}Zn with the yrast and yrare $I = 0\hbar, 2\hbar, 4\hbar, 6\hbar$ cascades. ND2 is accompanied by a signature $\alpha = 1$ sequence of $I = 3\hbar, 5\hbar, 7\hbar$ states with $E2$ transitions amongst them and mixed $E2/M1$ transitions connecting to the even-spin states of ND2.

TABLE I. The energies of excited states in ^{62}Zn, the transitions energies and relative intensities of the γ rays placed in the level scheme, the DCO ratios of three different angle combinations, the deduced mixing ratios, and the spins and parities of the initial and final states of the γ rays.

E_x (keV)	E_γ (keV)	I_{rel} (10^{-4})	Gate[a] X^Y	R_{DCO} 30°–83°	R_{DCO} 30°–53°	R_{DCO} 53°–83°	$\delta(E2/M1)$	Multipolarity assignment	I_i^π ($\hbar$)	I_f^π ($\hbar$)
				ND1-ND7						
954.0(3)	953.9(3)	10 000(300)	1232	0.93(4)				$E2$	$2^{+\,\text{b}}$	0^+
1804.7(3)	850.9(3)	980(29)	1604	0.93(6)				$\Delta I = 0$	$2^{+\,\text{b}}$	2^+
	1805.0(5)	851(44)	1604	1.12(9)				$E2$	2^+	0^+
2186.2(3)	1231.9(3)	8780(260)	954	1.12(5)				$E2$	$4^{+\,\text{b}}$	2^+
2384.6(3)	580.1(2)	205(6)	1604	0.36(7)	0.57(8)	0.68(5)	$\approx 0.15; \approx 2.1$	$E2/M1$	$3^{+\,\text{b}}$	2^+
	1430.6(6)	277(14)	1557	0.84(9)	1.05(9)	0.95(8)	$-0.30(^7_6)$	$E2/M1$	3^+	2^+
2743.8(3)	359.5(2)	171(5)	1604	0.39(4)	0.74(7)	0.70(5)	$0.13(^{10}_7)$	$E2/M1$	$4^{+\,\text{b}}$	3^+
	557.3(3)	1730(130)	1604	0.80(5)[c]				$\Delta I = 0$	4^+	4^+
	938.4(4)	987(43)	1604	0.98(5)				$E2$	4^+	2^+
3209.9(4)	1023.4(5)	42(5)	1177	0.50(18)				$E1$	$3^{-\,\text{b}}$	4^+
	2256.1(16)	12(2)						$E1$	3^-	2^+
3586.9(4)	843.2(3)	374(19)	1557	0.28(2)	0.58(5)	0.54(4)	$\approx 0.39; \approx 1.9$	$E2/M1$	$5^{+\,\text{b}}$	4^+
	1202.2(5)	355(18)	1557	1.04(6)				$E2$	5^+	3^+
	1400.7(11)	8(2)						$E2/M1$	5^+	4^+
3707.7(3)	1521.6(4)	6240(190)	954	1.14(5)				$E2$	$6^{+\,\text{b}}$	4^+
4043.2(4)	833.3(3)	56(4)	1177	1.03(19)				$E2$	$5^{-\,\text{b}}$	3^-
	1299.4(5)	187(9)	1177	0.63(6)				$E1$	5^-	4^+
	1857.4(7)	598(27)	1232	0.66(4)				$E1$	5^-	4^+
4231.1(6)	643.9(8)	7(1)						$\Delta I = 0$	$5^{+\,\text{d}}$	5^+
	1487.1(15)	5(1)						$E2/M1$	5^+	4^+
	1845.8(17)	8(3)						$E2$	5^+	3^+
	2044.8(18)	8(1)						$E2/M1$	5^+	4^+
4348.2(4)	640.6(2)	360(11)	1522	0.95(8)				$\Delta I = 0$	$6^{+\,\text{b}}$	6^+
	761.4(2)	261(8)	1202	0.53(6)	0.66(9)	0.73(7)	$0.07(^{10}_8)$	$E2/M1$	6^+	5^+
	1604.4(4)	2650(90)	954	1.19(5)[c]				$E2$	6^+	4^+
4535.4(4)	492.4(2)	39(5)						$\Delta I = 0$	5^-	5^-
	827.7(4)	57(7)	1522	0.39(11)				$E1$	5^-	6^+
	2349.8(9)	190(14)	1232	0.64(5)[c]				$E1$	5^-	4^+
4904.9(4)	369.7(2)	248(7)	1177	0.92(7)				$E2$	$7^{-\,\text{b}}$	5^-
	556.9(5)	2480(130)	1522	0.59(3)				$E1$	7^-	6^+
	861.4(3)	259(8)	1177	1.01(11)				$E2$	7^-	5^-
	1196.8(6)	5310(160)	1177	0.57(2)				$E1$	7^-	6^+
5124.1(4)	219.3(2)	42(3)	1507	0.87(11)				$\Delta I = 0$	$7^{-\,\text{b}}$	7^-
	775.8(7)	9(1)						$E1$	7^-	6^+
	1080.4(4)	543(22)	1507	1.14(8)				$E2$	7^-	5^-
	1416.8(6)	148(10)	1507	0.53(7)				$E1$	7^-	6^+
5131.4(5)	1088.0(4)	133(8)	1309	0.32(5)	0.71(8)	0.38(6)	$0.1 < \delta < 3.1$	$E2/M1$	$6^{-\,\text{b}}$	5^-
5144.0(4)	795.8(3)	113(8)	1604	0.39(9)	0.65(12)	0.58(10)	$0.23(^{32}_{13}); 2.6(^{19}_{10})$	$E2/M1$	7^+	6^+
	1557.2(6)	324(15)	1072	1.12(10)				$E2$	7^+	5^+
5481.4(6)	1773.8(7)	491(34)	1232	1.10(8)				$E2$	$8^{+\,\text{b}}$	6^+
5693.4(8)	1650.9(12)	21(2)	1857	0.94(29)				$E2$	7^-	5^-
	1985.1(16)	17(4)	1522	0.41(17)				$E1$	7^-	6^+
5878.8(8)	2171.0(9)	35(4)								6^+
5910.7(5)	1562.8(9)	6(2)						$E2$	$8^{+\,\text{d}}$	6^+
	2203.2(11)	28(3)						$E2$	8^+	6^+
6081.7(5)	171.0(3)	17(3)						$E1$	$9^{-\,\text{b}}$	8^+
	1176.7(4)	7710(230)	1791	1.03(5)				$E2$	9^-	7^-
6113.7(5)	981.8(4)	86(7)	1602	1.30(32)				$E2$	$8^{-\,\text{b}}$	6^-
	990.2(6)	21(4)	1309	0.62(9)				$E2/M1$	8^-	7^-
	1208.8(5)	626(28)	1309	0.96(5)	1.19(6)	0.86(5)	$-0.35(5); -2.8(^4_5)$	$E2/M1$	8^-	7^-
6304.5(6)	1160.8(11)	9(4)						$\Delta I = 0$	$7^{+\,\text{d}}$	7^+
	1954.9(17)	8(1)						$E2/M1$	7^+	6^+

TABLE I. (*Continued.*)

E_x (keV)	E_γ (keV)	$I_{\rm rel}$ (10^{-4})	Gate[a] X^Y	$R_{\rm DCO}$ 30°–83°	30°–53°	53°–83°	$\delta(E2/M1)$	Multipolarity assignment	I_i^π $(\hbar)$	I_f^π $(\hbar)$
	2073.0(12)	13(1)						$E2$	7^+	5^+
	2597.6(17)	13(1)						$E2/M1$	7^+	6^+
	2716.3(16)	23(1)	1072	0.94(16)				$E2$	7^+	5^+
6343.0(7)	1219.0(7)	85(4)	1080	0.31(3)	0.67(5)	0.57(4)	$0.22(^{12}_{8})$;2.3(6)	$E2/M1$	8^-	7^-
6444.9(10)	2097.1(12)	45(3)	1604	0.81(34)				$(E2)$	(8^+)	6^+
6631.1(5)	549.6(8)	8(1)						$\Delta I = 0$	$9^{-\,\text{b}}$	9^-
	720.5(10)	11(1)						$E1$	9^-	8^+
	1507.2(6)	411(21)	1080	1.05(6)				$E2$	9^-	7^-
6964.8(6)	1085.8(11)	16(3)							9^+	
	1483.3(13)	8(2)						$E2/M1$	9^+	8^+
	1821.0(10)	74(5)	1557	1.15(8)				$E2$	9^+	7^+
7024.3(8)	1331.2(9)	41(5)	1480	0.97(7)[c]				$(E2)$	(9^-)	7^-
	1543.1(13)	18(4)	1774	0.40(10)[c]				$(E1)$	(9^-)	8^+
7422.4(5)	1340.4(4)	6580(210)	1177	1.05(5)				$E2$	$11^{-\,\text{b}}$	9^-
7422.9(5)	791.7(8)	11(1)	1701	0.44(10)				$E2/M1$	$10^{-\,\text{b}}$	9^-
	1309.3(5)	584(37)	1701	0.97(5)				$E2$	10^-	8^-
	1341.4(7)	203(36)	1701	0.94(7)[c]				$E2/M1$	10^-	9^-
7444.9(6)	1331.1(9)	14(3)						$E2/M1$	9^-	8^-
	1363.3(5)	29(2)	1639	1.13(12)				$\Delta I = 0$	9^-	9^-
7499.2(8)	2017.8(9)	159(8)	1774	1.03(8)				$E2$	$10^{+\,\text{b}}$	8^+
7739.1(6)	1108.2(4)	108(4)	1080	0.55(6)				$E2/M1$	10^-	9^-
	1396.4(10)	55(3)	1080	0.88(9)				$E2$	10^-	8^-
7975.6(5)	1011.0(9)	8(1)						$\Delta I = 0$	$9^{+\,\text{b}}$	9^+
	1531.2(13)	8(1)						$(E2/M1)$	9^+	(8^+)
	1632.6(12)	33(5)	1072	0.66(38)				$E1$	9^+	8^-
	1670.4(7)	45(2)	1072	1.32(22)				$E2$	9^+	7^+
	1862.2(13)	24(3)	1072	0.66(7)				$E1$	9^+	8^-
	1894.2(8)	46(3)	1072	1.01(13)				$\Delta I = 0$	9^+	9^-
	2065.0(18)	17(3)	1072	0.83(14)				$E2/M1$	9^+	8^+
	2831.9(14)	104(9)	1072	1.16(10)				$E2$	9^+	7^+
7985.0(7)	961.0(9)	51(6)	911	0.42(9)				$(E1)$	10^+	(9^-)
	1353.6(12)	9(3)						$E1$	10^+	9^-
	1902.7(17)	16(5)						$E1$	10^+	9^-
8437.1(6)	1806.0(17)	9(2)						$E1$	$10^{+\,\text{b}}$	9^-
	2354.9(12)	328(19)	1028	0.67(5)				$E1$	10^+	9^-
8480.1(6)	1056.1(6)	25(3)	1340	0.57(15)				$\Delta I = 1$	10	11^-
	1515.3(15)	8(2)						$\Delta I = 1$	10	9^+
	2398.3(17)	14(2)						$\Delta I = 1$	10	9^-
8489.9(8)	1859.0(11)	121(5)	1080	0.74(5)[c]				$(E2)^{\text{e,f}}$	(11^-)	9^-
9024.6(6)	1601.7(7)	483(37)	1309	1.02(6)[c]				$E2$	12^-	10^-
	1602.7(8)	211(24)	1701	0.82(5)[c]				$E2/M1$	12^-	11^-
9047.9(5)	566.6(6)	27(3)	911	0.68(8)				$\Delta I = 1$	$11^{+\,\text{b}}$	10
	610.9(6)	26(3)	911	0.42(12)				$E2/M1$	11^+	10^+
	1072.2(7)	290(11)	911	1.08(6)				$E2$	11^+	9^+
	1310.0(8)	50(4)						$E1$	11^+	10^-
	1625.0(9)	149(6)	911	0.59(4)				$E1$	11^+	10^-
	1548.6(12)	11(2)	911	0.58(18)				$E2/M1$	11^+	10^+
	2083.0(18)	13(1)	911					$E2$	11^+	9^+
9083.6(6)	603.2(7)	16(3)	1177					$\Delta I = 1$	11^-	10
	1638.7(8)	67(5)	1177	0.93(7)[c]				$E2$	11^-	9^-
	1661.7(10)	35(4)						$\Delta I = 0$	11^-	11^-
	3002.1(12)	54(3)						$E2$	11^-	9^-
9213.8(6)	1791.3(6)	3760(130)	1177	1.08(5)				$E2$	$13^{-\,\text{b}}$	11^-
9464.8(5)	416.9(2)	151(5)	1586	0.44(9)[c]				$E2/M1$	$12^{+\,\text{b}}$	11^+
	974.8(10)	15(3)						$E1$	12^+	11^-
	1027.6(4)	216(11)	1586	0.90(10)				$E2$	12^+	10^+

TABLE I. (*Continued.*)

E_x (keV)	E_γ (keV)	I_{rel} (10^{-4})	Gate[a] X^Y	R_{DCO} 30°–83°	30°–53°	53°–83°	$\delta(E2/M1)$	Multipolarity assignment	I_i^π (ℏ)	I_f^π (ℏ)
	1479.8(9)	83(6)	1586	0.96(16)				$E2$	12^+	10^+
	1965.5(18)	9(2)						$E2$	12^+	10^+
	2042.5(11)	432(18)	1586	0.51(5)				$E1$	12^+	11^-
9681.8(11)	1192.7(13)	11(1)						$E2/M1$	12^-	(11^-)
	1942.0(14)	18(2)	1080	0.97(17)				$E2$	12^-	10^-
9822.9(8)	2401.7(9)	290(9)	1724	0.63(6)				$E1$	12^{+d}	11^-
9866.0(9)	2442.9(13)	45(1)	1353	0.46(10)				$E1$	11^+	10^-
9959.9(6)	495.1(5)	14(2)						$E2/M1$	13^+	12^+
	911.2(8)	381(18)	1072	1.08(6)				$E2$	13^+	11^+
	935.7(8)	119(6)	1309	0.72(5)				$E1$	13^+	12^-
10 374.7(6)	414.8(4)	27(2)	1586	0.44(9)[c]				$E2/M1$	14^{+b}	13^+
	909.6(6)	463(19)	1028	1.01(8)				$E2$	14^+	12^+
	1160.9(5)	2710(90)	1586	0.54(3)				$E1$	14^+	13^-
10 456.9(13)	1966.9(15)	107(7)	1080	1.12(11)				$E2$	(13^-)	(11^-)
10 725.4(7)	1511.6(7)	57(6)	1791	0.59(5)	0.91(8)	0.86(6)	$-0.11\binom{6}{5}$	$E2/M1$	14^-	13^-
	1701.0(9)	292(13)	1309	1.09(6)				$E2$	14^-	12^-
11 546.0(7)	1723.7(7)	112(5)	1340	1.09(6)				$E2$	14^+	12^+
	2333.1(13)	62(4)	1791	0.53(9)				$E1$	14^+	13^-
11 786.7(10)	1826.7(9)	348(14)	911	1.07(4)				$E2$	15^+	13^+
11 961.1(7)	1586.4(5)	2170(70)	1340	1.05(5)[c]				$E2$	16^{+b}	14^+
12 046.2(15)	1589.2(13)	32(3)						$(E2/M1)^{e,f}$	(14^-)	13^-
	2364.5(19)	9(1)						$(E2)$	(14^-)	12^-
12 276.7(8)	1901.8(7)	245(15)	1791	0.35(3)	0.55(6)	0.43(4)	$0.26\binom{9}{7}; 2.5\binom{7}{6}$	$E2/M1$	15^+	14^+
12 812.4(7)	1266.9(5)	80(5)	1633	0.64(9)				$E1$	15^{-b}	14^+
	2355.4(20)	6(2)						$E2$	15^-	13^-
	2436.9(9)	482(22)	1340	0.68(4)				$E1$	15^-	14^+
	3597.1(22)	11(1)						$E2$	15^-	13^-
12 831.5(18)	2374.6(14)	25(2)						$(E2)^e$	(15^-)	(13^-)
13 156.3(8)	1610.3(10)	75(4)	1724	1.40(15)				$E2$	16^+	14^+
13 782.4(9)	1505.6(8)	63(3)	910	1.14(17)				$E2$	17^+	15^+
	1821.3(5)	283(16)	1586	0.35(3)	0.43(4)	0.45(4)	$0.26\binom{9}{7}; 1.7\binom{10}{7}$	$E2/M1$	17^+	16^+
14 343.9(12)	3618.4(10)	17(2)	1701	0.95(19)				$(E2)$	(16^-)	14^-
14 444.9(6)	718.8(3)	112(5)	1396	0.55(6)	0.92(9)	0.96(9)	$-0.10\binom{7}{6}$	$E2/M1$	17^{-b}	16^-
	1214.2(10)	12(1)						$E1$	17^-	16^+
	1288.8(8)	22(5)						$E1$	17^-	16^+
	1452.1(12)	10(1)						$E2$	17^-	15^-
	1632.8(7)	208(11)	1791	0.91(9)				$E2$	17^-	15^-
	2483.4(12)	492(30)	1586	0.52(3)				$E1$	17^-	16^+
14 567.8(22)	3842.4(21)	22(3)	1701	0.66(9)				$\Delta I = 1$	15	14^-
14 610.5(29)	4235.8(28)	25(5)								14^+
15 020.7(19)	3059.6(18)	37(2)	1586	0.75(10)				$\Delta I = 1$	17	16^+
15 682.1(25)	3721.0(24)	9(1)								16^+
15 704.6(7)	1259.6(4)	344(15)	1633	1.04(11)				$E2$	19^-	17^-
15 727.4(19)	1383.5(14)	13(1)								16^-
16 234.3(33)	4273.2(32)	17(1)	1586	0.58(10)				$\Delta I = 1$	17	16^+
16 413.9(27)	4452.8(26)	13(2)								16^+
16 874.2(25)	3091.8(23)	11(2)								17^+
17 035.1(33)	5074.0(32)	11(2)								16^+
17 400.1(28)	3617.7(27)	8(2)								17^+
17 665.9(26)	3883.5(25)	19(2)								17^+
17 748.8(32)	3966.4(31)	9(1)								17^+
17 843.5(43)	5882.4(42)	3(1)								16^+
18 020.3(35)	4237.9(34)	12(1)								16^+
18 592.6(37)	4810.2(36)	9(1)								17^+
19 177.0(25)	3472.4(24)	12(1)								19^-
20 781.9(42)	5077.3(41)	5(1)								19^-

TABLE I. (*Continued.*)

E_x (keV)	E_γ (keV)	I_{rel} (10^{-4})	Gate[a] X^Y	R_{DCO} 30°–83°	30°–53°	53°–83°	$\delta(E2/M1)$	Multipolarity assignment	I_i^π ($\hbar$)	I_f^π ($\hbar$)
21 189.7(49)	5485.1(42)	4(1)								19$^-$
23 024.2(46)	2242.3(19)	3(1)								
				TB1						
10 241.9(6)	1761.3(15)	13(2)						$\Delta I = 1$	11^{+}[b]	10
	1804.7(15)	14(3)						$E2/M1$	11$^+$	10$^+$
	2742.2(18)	34(4)	1774	1.10(16)				$E2/M1$	11$^+$	10$^+$
	2819.9(19)	27(3)	936	0.97(13)				$\Delta I = 0$	11$^+$	11$^-$
10 630.7(6)	388.8(4)	98(4)	1120	0.59(8)	0.93(15)	0.70(9)	$-0.06(^9_8)$	$E2/M1$	12^{+}[b]	11$^+$
	1547.2(6)	243(8)	1120	0.59(5)				$E1$	12$^+$	11$^-$
	1582.6(12)	13(2)						$E2/M1$	12$^+$	11$^+$
	2645.6(21)	12(3)						$E2$	12$^+$	10$^+$
	3132.1(19)	29(3)	1120	1.11(23)				$E2$	12$^+$	10$^+$
	3208.4(18)	63(3)	1120	0.54(8)				$E1$	12$^+$	11$^-$
11 177.9(6)	547.2(2)	505(13)	1353	0.71(4)	0.92(5)	0.79(4)	$-0.16(4)$	$E2/M1$	13^{+}[b]	12$^+$
	936.1(7)	107(5)	TB1	0.86(7)				$E2$	13$^+$	11$^+$
	1311.8(9)	33(4)						$E2$	13$^+$	11$^+$
	1712.2(13)	19(4)						$E2/M1$	13$^+$	12$^+$
	2154.0(14)	55(4)	1353	0.43(7)[c]				$E1$	13$^+$	12$^-$
11 751.2(6)	573.3(2)	448(13)	TB1	0.63(5)	0.90(7)	0.80(4)	$-0.12(^5_4)$	$E2/M1$	14^{+}[b]	13$^+$
	1120.0(11)	294(8)	TB1	1.29(12)				$E2$	14^{+}[b]	12$^+$
	2286.6(18)	16(3)						$E2$	14$^+$	12$^+$
	2537.4(14)	121(8)	1480	0.59(11)[c]				$E1$	14$^+$	13$^-$
12 531.6(6)	780.4(3)	537(16)	1120	0.64(5)	1.09(10)	0.82(6)	$-0.15(^6_5)$	$E2/M1$	15^{+}[b]	14$^+$
	1353.3(8)	427(14)	1588	1.01(5)				$E2$	15$^+$	13$^+$
	2156.9(17)	36(5)						$E2/M1$	15$^+$	14$^+$
13 231.1(6)	699.4(3)	501(15)	1353	0.69(4)	0.84(5)	0.73(5)	$-0.11(^5_4)$	$E2/M1$	16^{+}[b]	15$^+$
	1479.6(7)	687(22)	1120	1.04(12)				$E2$	16$^+$	14$^+$
	2856.2(21)	39(4)						$E2$	16$^+$	14$^+$
14 119.1(7)	888.0(4)	296(9)	1480	0.68(7)	0.92(8)	0.85(5)	$-0.18(^6_5)$	$E2/M1$	17^{+}[b]	16$^+$
	1587.7(10)	195(6)	TB1	1.28(11)[c]				$E2$	17$^+$	15$^+$
	2157.7(20)	42(5)	1586	0.74(9)[c]				$E2/M1$	17$^+$	16$^+$
15 042.7(7)	923.6(5)	233(8)	1588	0.67(6)	1.01(8)	0.81(6)	$-0.18(5)$	$E2/M1$	18^{+}[b]	17$^+$
	1811.3(8)	261(9)	1120	1.26(10)				$E2$	18$^+$	16$^+$
16 365.2(9)	1322.8(9)	181(12)	1811	0.47(6)	0.85(8)	0.76(8)	$-0.04(6)$	$E2/M1$	19^{+}[b]	18$^+$
	2245.3(15)	96(6)	1120	1.15(22)				$E2$	19$^+$	17$^+$
17 582.4(12)	1217.3(11)	65(5)	2245	0.76(12)				$E2/M1$	20^{+}[b]	19$^+$
	2539.7(14)	165(13)	1811	1.10(11)				$E2$	20$^+$	18$^+$
19 498.1(25)	3132.9(23)	26(2)						$(E2)$[f]	(21$^+$)	19$^+$
19 773.8(39)	4731.1(38)	8(2)								18$^+$
				TB2						
11 651.3(6)	1021.2(11)	8(3)						$E1$	13^{-}[b]	12$^+$
	2187.0(19)	9(2)						$E1$	13$^-$	12$^+$
	2436.1(16)	31(5)						$\Delta I = 0$	13$^-$	13$^-$
	2626.3(16)	31(2)						$E2/M1$	13$^-$	12$^-$
	4228.0(28)	59(6)	1340	1.30(21)				$E2$	13$^-$	11$^-$
12 329.2(6)	678.0(3)	143(5)	1396	0.72(6)	0.84(7)	0.90(8)	$-0.15(5)$	$E2/M1$	14^{-}[b]	13$^-$
	1151.6(7)	31(2)	1396	0.42(7)				$E1$	14$^-$	13$^+$
	1604.1(13)	16(5)						$\Delta I = 0$	14$^-$	14$^-$
	2369.4(17)	23(4)						$E1$	14$^-$	13$^+$
	3115.2(18)	240(19)	1396	0.93(10)				$E2/M1$	14$^-$	13$^-$
	3304.9(14)	11(2)						$E2$	14$^-$	12$^-$
12 992.7(6)	663.7(3)	527(16)	1548	0.61(4)	0.88(5)	0.81(5)	$-0.12(4)$	$E2/M1$	15^{-}[b]	14$^-$
	1241.4(7)	105(6)	1548	0.54(6)				$E1$	15$^-$	14$^+$
	1341.4(8)	163(51)	1688	1.01(8)[c]				$E2$	15$^-$	13$^-$
	1446.8(10)	14(2)						$E1$	15$^-$	14$^+$
	3779.3(29)	18(4)	1791	0.85(18)				$E2$	15$^-$	13$^-$

TABLE I. (*Continued.*)

E_x (keV)	E_γ (keV)	I_{rel} (10^{-4})	Gate[a] X^Y	R_{DCO} 30°–83°	30°–53°	53°–83°	$\delta(E2/M1)$	Multipolarity assignment	I_i^π ($\hbar$)	I_f^π ($\hbar$)
13 726.0(6)	733.5(3)	662(15)	1688	0.60(4)	0.82(5)	0.74(5)	$-0.07(^4_3)$	$E2/M1$	16^{-b}	15^-
	913.6(5)	57(5)	1688	0.67(8)	0.94(10)	0.96(12)	$-0.16(6)$	$E2/M1$	16^-	15^-
	1193.9(9)	53(8)	1688	0.62(6)[c]				$E1$	16^-	15^+
	1396.4(7)	634(21)	1688	0.97(7)				$E2$	16^-	15^-
14 540.9(6)	814.9(4)	469(15)	1396	0.64(4)	0.92(5)	0.77(4)	$-0.14(4)$	$E2/M1$	17^{-b}	16^-
	1309.6(9)	91(5)	2064	0.59(5)[c]				$E1$	17^-	16^+
	1384.2(10)	21(3)						$E1$	17^-	16^+
	1548.3(7)	581(22)	2064	1.18(15)				$E2$	17^-	15^-
	2580.7(14)	186(7)	2064	0.69(6)				$E1$	17^-	16^+
15 414.1(7)	873.2(4)	312(10)	2064	0.72(4)	0.88(5)	0.77(5)	$-0.16(4)$	$E2/M1$	18^{-b}	17^-
	969.3(6)	189(6)	2064	0.69(6)	1.08(9)	0.68(7)	$-0.19(10); -6.8(^{13}_{53})$	$E2/M1$	18^-	17^-
	1295.0(8)	67(5)						$E1$	18^-	17^+
	1688.4(7)	706(25)	2064	0.96(4)				$E2$	18^-	16^-
16 372.7(7)	959.0(5)	359(16)	1688	0.77(7)[c]	0.86(8)	0.84(8)	$-0.19(^8_7)$	$E2/M1$	19^-	18^-
	1329.6(9)	37(3)						$E1$	19^-	18^+
	1831.4(8)	506(16)	TB2	1.15(10)				$E2$	19^-	17^-
	1927.6(10)	222(8)	1633	1.14(10)				$E2$	19^-	17^-
17477.8(8)	1105.1(6)	345(13)	1688	0.69(13)				$E2/M1$	20^{-b}	19^-
	1112.6(12)	9(1)						$E1$	20^-	19^+
	2063.8(10)	503(17)	TB2	1.00(8)				$E2$	20^-	18^-
18 502.0(9)	1024.6(6)	101(5)	2064	0.85(6)	0.82(6)	0.67(5)	$-0.18(9)$	$E2/M1$	21^{-b}	20^-
	2129.1(11)	437(14)	TB2	1.04(10)				$E2$	21^-	19^-
19 676.4(10)	1174.8(6)	99(6)	TB2	[c]				$E2/M1$	22^{-b}	21^-
	2197.0(13)	171(8)	TB2	1.03(11)				$E2$	22^-	20^-
20 026.7(24)	3654.2(30)	15(2)								19^-
	4321.8(37)	5(2)								19^-
21 036.8(11)	1360.2(5)	72(4)	TB2	0.53(7)[c]				$E2/M1$	23^{-b}	22^-
	2535.0(13)	163(6)	TB2	0.98(14)				$E2$	23^-	21^-
21 196.7(32)	3719.2(31)	21(1)	TB2	0.61(19)				$\Delta I = 1$	21	20^-
21 316.1(30)	3838.3(29)	24(2)	TB2	0.73(10)				$\Delta I = 1$	21	20^-
21 401.3(30)	3923.5(29)	35(2)	TB2	0.96(10)				$(E2)$	(22^-)	20^-
22 741.3(41)	4239.3(40)	10(2)								21^-
22 822.4(34)	4320.4(33)	15(2)								21^-
23 079.2(27)	3402.7(25)	21(2)								22^-
23 179.0(16)	2142.2(16)	27(2)							$E2/M1$	24^{-b}	23^-
	3502.7(21)	65(5)	TB2	1.33(19)				$E2$	24^-	22^-
23 184.2(39)	4682.2(38)	8(2)								21^-
23 407.8(44)	4905.8(43)	6(1)								21^-
23 761.3(45)	5259.3(44)	4(1)								21^-
24 307.7(38)	4631.2(37)	18(2)	TB2	1.26(14)[c]				$(E2)$	$(24)^-$	22^-
25 438.1(40)	4401.3(38)	5(1)								23^-
25 660.2(33)	4623.4(26)	20(3)	TB2	1.16(15)				$E2$	25^-	23^-
25 880.1(38)	4843.3(36)	11(1)								23^-
25 989.4(41)	4952.7(39)	8(1)								23^-
26 227.9(43)	5191.1(41)	8(1)								23^-
				WD1						
14 644.6(14)	2858.3(20)	22(3)						$E2/M1$	16^{+d}	15^+
14 831.2(13)	3043.5(21)	24(4)						$E2/M1$	16^{+d}	15^+
15 040.3(12)	3494.8(25)	7(1)						$E2$	16^{+d}	14^+
16 469.8(16)	4508.6(28)	29(2)	1586	0.86(18)				$E2^d$	18^+	16^+
16 715.2(11)	1675.3(11)	20(2)						$E2$	18^+	16^+
	1883.7(10)	28(3)	WD1a	1.27(10)				$E2$	18^+	16^+
	2070.7(12)	51(3)	2180	1.11(13)				$E2$	18^+	16^+
	2270.5(17)	11(1)						$E2$	18^+	16^+
	4752.4(38)	13(2)	WD1a	1.36(18)				$E2$	18^+	16^+

TABLE I. (*Continued.*)

E_x (keV)	E_γ (keV)	$I_{\rm rel}$ (10^{-4})	Gate[a] X^Y	$R_{\rm DCO}$ 30°–83°	30°–53°	53°–83°	$\delta(E2/M1)$	Multipolarity assignment	I_i^π $(\hbar)$	I_f^π $(\hbar)$
16 817.4(12)	1776.9(8)	65(4)	WD1b	1.04(14)				$E2$	18^+	16^+
	1832.7(9)	38(3)							18^+	
	2372.7(19)	12(1)						$E1$	18^+	17^-
	4856.4(32)	13(2)						$E2$	18^+	16^+
18 677.3(12)	1859.7(10)	105(5)	WD1b	0.90(7)[c]				$E2$	20^+	18^+
	1962.3(11)	97(4)	WD1b	1.09(10)				$E2$	20^+	18^+
	2207.0(18)	9(2)						$E2$	20^+	18^+
	2972.8(25)	8(2)						$E1$	20^+	19^-
20 857.1(17)	2179.8(12)	195(7)	WD1b	1.04(10)				$E2$	22^+	20^+
23 341.7(22)	2484.6(14)	185(6)	WD1b	0.95(10)				$E2$	24^+	22^+
26 173.9(30)	2832.2(20)	85(4)	WD1b	0.94(9)				$E2$	26^+	24^+
29 473.7(40)	3299.8(26)	35(3)	WD1b	1.17(17)				$E2$	28^+	26^+
33 360.4(50)	3886.7(31)[g]	11(2)						$(E2)$[f]	(30^+)	28^+
33 790.5(52)	4316.8(34)[g]	9(2)						$(E2)$[f]	(30^+)	28^+
				WD2						
13 964.4(13)	3589.7(17)	41(3)	910	1.46(37)				$(E2)$	(16^+)	14^+
14 489.4(11)	4114.2(30)	12(1)	1791	0.69(15)				$E1$	15^-	14^+
	5275.0(35)	9(1)						$E2$	15^-	13^-
15 081.2(9)	2269.2(14)	16(2)						$E2/M1$	16^-	15^-
	2803.9(17)	17(1)						$E1$	16^-	15^+
	4355.4(26)	38(2)	1701/1602	1.06(9)				$E2$	16^-	14^-
15 750.2(8)	668.9(6)	17(2)						$E2/M1$	17^-	16^-
	1260.7(8)	78(6)	1966	1.09(10)				$E2$	17^-	15^-
	1306.0(11)	15(1)						$\Delta I = 0$	17^-	17^-
	1785.7(14)	13(1)						$(E1)$	17^-	(16^+)
	2518.6(17)	21(3)						$E1$	17^-	16^+
	3788.7(22)	23(1)	1586	0.49(9)				$E1$	17^-	16^+
16 500.7(9)	750.6(6)	11(1)						$E2/M1$	18^-	17^-
	1419.6(10)	98(9)	WD2b	1.01(15)				$E2$	18^-	16^-
17 338.8(9)	838.2(5)	19(2)	1966	0.83(14)				$E2/M1$	19^-	18^-
	1587.5(9)	109(8)	1966	1.00(5)[c]				$E2$	19^-	17^-
18 240.6(14)	2535.1(16)	41(3)	1260	0.43(6)				$E2/M1$	20^-	19^-
18 286.9(10)	948.1(10)	7(2)						$E2/M1$	20^-	19^-
	1786.3(9)	161(9)	WD2b	1.10(8)				$E2$	20^-	18^-
	2581.8(15)	42(3)	1260	0.75(10)				$E2/M1$	20^-	19^-
19 305.1(11)	1018.9(11)	9(1)						$E2/M1$	21^-	20^-
	1966.4(10)	173(7)	WD2a	1.10(10)				$E2$	21^-	19^-
20 442.0(12)	1136.8(11)	7(2)						$E2/M1$	22^-	21^-
	2155.4(13)	172(7)	WD2b	1.00(10)				$E2$	22^-	20^-
	2201.6(17)	31(2)	WD2b	0.98(8)				$E2$	22^-	20^-
21 682.5(14)	1240.5(13)	6(2)						$E2/M1$	23^-	22^-
	2377.3(13)	117(5)	WD2a	0.94(9)				$E2$	23^-	21^-
23 072.1(16)	1388.4(14)	12(2)						$E2/M1$	24^-	23^-
	2630.2(15)	162(8)	WD2b	1.04(10)				$E2$	24^-	22^-
24 607.1(22)	2924.6(17)	95(5)	WD2a	1.21(11)				$E2$	25^-	23^-
26 323.4(24)	3251.3(18)	77(4)	WD2b	0.90(9)				$E2$	26^-	24^-
28 229.7(40)	3622.6(33)	18(2)	WD2a	1.00(10)				$E2$	27^-	25^-
30 508.3(44)	4185.0(37)	5(1)						$(E2)$[f]	(28^-)	26^-
				WD3						
15 076.7(11)	1580.1(18)	11(2)						$(E2)$[f]	17^-	(15^-)
	2264.7(17)	8(2)						$E2$	17^-	15^-
	3116.2(18)	33(2)	1586	0.67(7)				$\Delta I = 1$	17^-	16^+
16 901.4(11)	1196.0(13)	9(3)						$\Delta I = 0$	19^-	19^-
	1824.7(11)	95(4)	WD3	0.92(8)[c]				$E2$	19^-	17^-
	2456.2(20)	15(4)						$E2$	19^-	17^-

TABLE I. (*Continued.*)

E_x	E_γ	I_{rel}	Gate[a]	R_{DCO}			$\delta(E2/M1)$	Multipolarity	I_i^π	I_f^π
(keV)	(keV)	(10^{-4})	X^Y	30°–83°	30°–53°	53°–83°		assignment	$(\hbar)$	$(\hbar)$
19 093.2(16)	2192.0(12)	101(5)	WD3	0.97(10)				$E2$	21^-	19^-
21687.0(22)	2593.8(14)	75(4)	WD3	1.17(8)				$E2$	23^-	21^-
24 725.6(28)	3038.6(18)	39(3)	WD3	1.03(16)				$E2$	25^-	23^-
28 555.1(42)	3829.5(31)	7(2)						$(E2)^f$	(27^-)	25^-
				WD4 and WD5						
15 281.3(14)	2050.6(17)	8(1)	2208	$0.66(12)^c$				$E2/M1$	17^+	16^+
	3495.4(29)	7(1)	WD5	1.22(26)				$E2$	17^+	15^+
15 407.6(18)	3618.7(30)	4(1)						$E2^d$	17^+	15^+
15 716.2(18)	3438.8(28)	6(1)						$E2^d$	17^+	15^+
	3754.6(29)	5(1)						$E2/M1^d$	17^+	16^+
	3930.4(31)	8(1)						$E2^d$	17^+	15^+
17 488.7(16)	2080.8(11)	13(2)						$E2^d$	19^+	17^+
	2207.9(14)	24(4)	WD5	0.93(14)				$E2$	19^+	17^+
17 696.8(18)	1980.6(11)	16(2)						$E2^d$	19^+	17^+
18 516.4(25)	4734.0(28)	13(2)	WD4	1.20(25)				$E2$	19^+	17^+
20 086.2(17)	2389.4(14)	26(2)	WD5	0.98(12)				$E2$	21^+	19^+
	2597.4(13)	34(3)	WD5	0.95(19)				$E2$	21^+	19^+
20 432.2(26)	1915.8(11)	52(4)	WD4	0.99(19)				$E2$	21^+	19^+
20 658.4(25)	1933.7(13)	17(4)						$(E2)^f$	21^+	(19^+)
22 567.7(28)	2135.5(14)	34(3)	WD4	1.06(10)				$E2$	23^+	21^+
22 794.2(23)	2135.9(15)	6(2)							23^+	21^+
	2173.8(11)	22(2)						$(E2)^f$	23^+	(21^+)
	2707.8(22)	30(2)	WD5	0.96(15)				$E2$	23^+	21^+
22 865.9(23)	2207.3(15)	42(5)	2472	0.99(18)				$E2$	23^+	21^+
	2780.1(24)	19(2)	WD5	1.29(40)				$E2$	23^+	21^+
25 145.1(29)	2577.4(16)	16(2)	WD4	1.04(19)				$E2$	25^+	23^+
25 338.4(23)	2472.4(13)	28(3)	2208	1.08(18)				$E2$	25^+	23^+
	2544.2(12)	45(3)	WD5	0.94(19)				$E2$	25^+	23^+
28 205.4(28)	2867.1(24)	29(3)	WD5	0.98(14)				$E2$	27^+	25^+
	3060.4(25)	6(2)						$E2$	27^+	25^+
31 542.3(40)	3336.9(29)	9(2)						$(E2)^f$	(29^+)	27^+
35 338.3(55)	$3796.0(38)^g$	2(1)						$(E2)^f$	(31^+)	(29^+)
				WD6 and WD7						
15 870.4(20)	3908.9(31)	4(1)						$(E1)$	(17^-)	16^+
16 102.1(16)	2870.8(22)	7(2)						$E1^d$	17^-	16^+
	4141.0(29)	17(2)	1586	0.51(10)				$E1$	17^-	16^+
17 579.3(19)	1709.1(17)	9(2)						$(E2)^f$	19^-	(17^-)
	3134.4(26)	18(4)	2178	1.08(31)				$E2$	19^-	17^-
17 764.5(17)	1662.4(10)	60(4)	WD6	1.15(10)				$E2$	19^-	17^-
19 486.3(19)	3780.8(25)	29(3)	1260	1.19(27)				$E2$	21^-	19^-
19 757.7(19)	2178.6(13)	45(4)	WD5	1.14(10)				$E2$	21^-	19^-
19 778.1(18)	2013.5(13)	72(5)	WD6	1.12(11)				$E2$	21^-	19^-
22 127.6(18)	2349.5(13)	33(2)	WD6	1.13(13)				$E2$	23^-	21^-
	2370.0(11)	40(3)	WD5	1.13(7)				$E2$	23^-	21^-
	2640.7(22)	7(2)						$E2$	23^-	21^-
22 243.9(19)	2465.7(14)	43(3)	WD6	1.08(17)				$E2$	23^-	21^-
	2486.8(21)	3(1)						$E2$	23^-	21^-
	2757.4(23)	6(2)						$E2$	23^-	21^-
24 913.1(24)	2785.5(16)	58(4)	WD5	0.93(14)				$E2$	25^-	23^-
25 162.4(26)	2918.5(17)	32(2)	WD6	0.86(13)				$E2$	25^-	23^-
28 369.4(35)	3456.4(25)	23(3)	WD5	1.27(46)				$(E2)$	(27^-)	25^-
28 745.6(42)	3583.1(33)	5(2)						$(E2)^f$	(27^-)	25^-
				WD8						
17 646.1(39)	1850.2(16)	11(2)						$(E2)^f$	(18^+)	(16^+)
	5685.0(38)	6(1)						$(E2)^e$	(18^+)	16^+
19 702.5(41)	2056.4(14)	53(6)	WD7	$1.16(16)^c$				$E2$	(20^+)	(18^+)

TABLE I. (*Continued.*)

E_x (keV)	E_γ (keV)	$I_{\rm rel}$ (10^{-4})	Gate[a] X^Y	$R_{\rm DCO}$ 30°–83°	30°–53°	53°–83°	$\delta(E2/M1)$	Multipolarity assignment	I_i^π $(\hbar)$	I_f^π $(\hbar)$
22 029.9(44)	2327.0(15)	43(4)	WD7	1.18(10)[c]				$E2$	(22^+)	(20^+)
24 692.2(47)	2662.3(18)	30(2)	WD7	1.04(26)				$E2$	(24^+)	(22^+)
27 763.7(55)	3071.5(28)	7(1)						$(E2)^{\rm f}$	(26^+)	(24^+)
				WD9						
16 368.8(46)	2047.7(20)	8(2)							$(17)^{\rm f}$	
16 443.2(39)	4482.1(38)	5(2)						$\Delta I = 1^{\rm e}$	(17)	16^+
18 505.0(43)	1828.0(17)	12(2)							(19)	
	2061.8(19)	11(2)						$(E2)^{\rm f}$	(19)	(17)
	2136.2(16)	18(2)						$(E2)^{\rm f}$	(19)	(17)
	4061.4(33)	4(2)						$(E2)^{\rm f}$	(19)	17^-
20 850.4(47)	2345.4(19)	31(2)						$(E2)^{\rm f}$	(21)	(19)
23 466.0(52)	2615.6(22)	27(2)						$(E2)^{\rm f}$	(23)	(21)
26 460.6(57)	2994.6(17)	14(1)						$(E2)^{\rm f}$	(25)	(23)
29 817.1(65)	3356.4(32)	4(1)						$(E2)^{\rm f}$	(27)	(25)
				WD10						
14 430.4(21)	4055.0(27)	48(4)	910	1.46(37)				$(E2)^{\rm e}$	(16^+)	14^+
16 323.9(22)	1893.4(11)	18(2)						$(E2)^{\rm f}$	(18^+)	(16^+)
18 759.4(21)	2290.1(20)	7(1)						$(E2)^{\rm f}$	(20^+)	18^+
	2435.3(15)	15(2)						$(E2)^{\rm f}$	(20^+)	(18^+)
21 403.6(29)	2644.2(20)	14(1)						$(E2)^{\rm f}$	(22^+)	(20^+)
21 468.4(30)	2709.0(21)	7(2)								(20^+)
23 625.4(34)	2221.8(18)	11(2)								(22^+)
				WD11						
15 829.8(24)	3869.0(27)	30(2)	1586	0.68(15)				$\Delta I = 1$	17	16^+
17 453.7(27)	1623.9(13)	16(2)								17
19 677.0(33)	2223.3(19)	12(3)								
				SD1						
17 365.1(18)	3638.7(33)	5(1)						$E2$	18^-	16^-
17 407.5(16)	2962.9(28)	6(1)	SD1	0.74(22)				$E2/M1$	18^-	17^-
	3682.0(34)	3(1)						$E2$	18^-	16^-
19 399.9(15)	1891.3(15)	12(1)						$(E2)^{\rm f}$	20^-	(18^-)
	1992.5(14)	18(1)	SD1					$E2^{\rm d}$	20^-	18^-
	2034.7(14)	15(2)						$E2^{\rm d}$	20^-	18^-
	2081.7(17)	9(1)						$(E2)^{\rm f}$	20^-	(18^-)
	3027.4(24)	8(2)						$E2/M1$	20^-	19^-
	3984.9(31)	11(1)	SD1	1.12(39)				$E2$	20^-	18^-
21 614.3(16)	2014.9(13)	13(2)						$(E2)^{\rm f}$	22^-	(20^-)
	2214.4(9)	106(8)	SD1	0.99(13)				$E2$	22^-	20^-
24 053.6(18)	2439.3(10)	131(7)	SD1	0.92(6)[c]				$E2$	24^-	22^-
	4377.1(34)	7(1)						$E2$	24^-	22^-
26 743.4(22)	2689.9(12)	81(6)	SD1	0.99(10)				$E2$	26^-	24^-
29 682.3(28)	2938.8(18)	28(2)	SD1	0.85(13)				$E2$	28^-	26^-
32 916.3(38)	3234.0(25)	7(2)						$(E2)^{\rm f}$	(30^-)	28^-
36 496.1(49)	3579.8(31)[g]	5(1)						$(E2)^{\rm f}$	(32^-)	(30^-)
40 454.4(61)	3958.3(37)[g]	3(1)						$(E2)^{\rm f}$	(34^-)	(32^-)
40 729.8(63)	4233.7(40)[g]	2(1)						$(E2)^{\rm f}$	(34^-)	(32^-)
				SD2 and SD5						
18 414.6(17)	1842.0(13)	6(1)						$(E2)^{\rm f}$	$19^{(-)}$	(17^-)
	2093.2(16)	4(1)						$(\Delta I = 1)$	$19^{(-)}$	(18^+)
	3002.9(26)	5(1)						$(E2/M1)$	$19^{(-)}$	18^-
20 472.3(18)	2057.8(12)	31(5)	SD2	1.02(21)				$E2$	$21^{(-)}$	$19^{(-)}$
	2994.0(30)	6(1)	SD2	0.61(20)				$\Delta I = 1$	$21^{(-)}$	20^-
22 781.5(19)	2309.2(14)	45(4)	SD2	0.98(20)				$E2$	$23^{(-)}$	$21^{(-)}$
	3105.5(29)	9(1)						$\Delta I = 1$	$23^{(-)}$	22^-
23 027.9(25)	4525.3(35)	24(2)	TB2	1.11(10)				$E2$	23^-	21^-

TABLE I. (*Continued.*)

E_x (keV)	E_γ (keV)	I_{rel} (10^{-4})	Gate[a] X^Y	R_{DCO} 30°–83°	30°–53°	53°–83°	$\delta(E2/M1)$	Multipolarity assignment	I_i^π (ℏ)	I_f^π (ℏ)
25 346.2(22)	2564.8(14)	50(5)	SD2	1.06(7)				$E2$	25$^{(-)}$	23$^{(-)}$
25 478.1(25)	2450.1(13)	18(2)						$(E2)^f$	(25$^-$)	23$^-$
28 161.8(25)	2683.7(19)	5(2)						$(E2)$	27$^{(-)}$	(25$^-$)
	2815.7(18)	26(3)	SD2	0.85(22)				$E2$	27$^{(-)}$	25$^{(-)}$
28 243.9(25)	2765.6(17)	7(2)						$(E2)^f$	(27$^-$)	(25$^-$)
	2897.7(21)	7(1)						$(E2)^f$	(27$^-$)	25$^{(-)}$
31 212.0(29)	2967.8(22)	3(2)						$(E2)^f$	(29$^-$)	(27$^-$)
	3050.6(23)	10(2)						$(E2)^f$	(29$^-$)	27$^{(-)}$
31 396.8(34)	3152.9(23)	8(2)						$(E2)^f$	(29$^-$)	(27$^-$)
34 599.6(39)	3387.6(26)^g	3(1)						$(E2)^f$	(31$^-$)	(29$^-$)
38 365.0(51)	3765.4(34)^g	2(1)						$(E2)^f$	(33$^-$)	(31$^-$)
42 517.6(65)	4152.6(39)^g	1(1)						$(E2)^f$	(35$^-$)	(33$^-$)
					SD3					
15 294.2(16)	2138.0(15)	13(2)						$E2$	18^{+d}	16$^+$
17 349.6(28)	1867.9(11)	31(3)	SD3	0.90(20)				$E2$	18$^+$	16$^+$
	5387.9(41)	17(2)	SD3	0.96(18)				$E2$	18$^+$	16$^+$
19 476.4(28)	2126.8(12)	75(5)	2375	0.92(9)				$E2$	20$^+$	18$^+$
	4183.5(31)	7(1)						$E2$	20$^+$	18$^+$
21 851.1(30)	2374.7(12)	77(6)	SD3	1.04(10)				$E2$	22$^+$	20$^+$
24 467.5(33)	2616.4(14)	52(4)	SD3	1.00(9)				$E2$	24$^+$	22$^+$
27 316.0(37)	2848.5(17)	23(3)	SD3	1.27(14)				$E2$	26$^+$	24$^+$
30 433.7(43)	3117.7(21)	10(1)	SD3	0.86(24)				$E2$	28$^+$	26$^+$
33 796.9(50)	3363.2(25)	3(1)	SD3					$(E2)^f$	(30$^+$)	28$^+$
					SD4					
21 602.3(47)	5897.7(46)	3(1)						$(E2)^e$	(21$^-$)	19$^-$
23 273.6(52)	2175.6(18)	17(3)							(22)	
23 376.4(49)	1551.8(13)	17(2)							(22)	
	1774.1(12)	12(2)	SD4	0.59(8)				$\Delta I = 1$	(22)	(21$^-$)
25 401.8(50)	2025.4(13)	41(3)	SD4	1.19(19)				$E2$	(24)	(22)
	2128.2(13)	38(4)	SD4	1.23(12)				$E2$	(24)	(22)
27 717.2(52)	2315.4(14)	97(5)	SD4	1.13(13)				$E2$	(26)	(24)
30 369.5(56)	2652.3(19)	58(4)	SD4	0.90(13)				$E2$	(28)	(26)
33 457.8(61)	3088.3(24)	21(3)						$(E2)^f$	(30)	(28)
36 896.3(68)	3438.4(32)^g	6(2)						$(E2)^f$	(32)	(30)

[a]Gate on the transitions: TB1, sum of 936, 1120, 1353, 1480, 1811, and 2245 keV; TB2, sum of 1396, 1548, 1688, 1831, 2064, and 2129 keV; WD1a, sum of 1962 and 2180 keV; WD1b, sum of 1860, 1962, 2180, 2485, and 2832 keV; WD2a, sum of 1261, 1588, 1966, and 2377 keV; WD2b, sum of 1420, 1786, 2155, and 2630 keV; WD3, sum of 1825, 2192, 2594, and 3039 keV; WD4, sum of 1916, 2136, and 2577 keV; WD5, sum of 2208, 2389, 2472, 2545, 2597, and 2708 keV; WD6, sum of 2179, 2370, and 2786 keV; WD7, sum of 1662, 2014, and 2466 keV; WD8, sum of 2056, 2327, and 2662 keV; SD1, sum of 1992, 2214, 2439, and 2690 keV; SD2, sum of 2058, 2309, 2565, and 2816 keV; SD3, sum of 2127, 2375, 2616, and 2848 keV; SD4, sum of 1552, 2025, 2315, and 2652 keV.

[b]Taken from or in accordance with published data.

[c]Doublet structure.

[d]Fixed owing to a stretched $E2$ cascade.

[e]Based on yrast arguments.

[f]Based on regular rotational structure.

[g]Transitions from data set 2.

At some 5 MeV excitation energy, the yrast line is determined by the negative-parity sequence ND3, which comprises nearly degenerate signature $\alpha = 1$ (favored in energy) and signature $\alpha = 0$ (unfavored) sequences up to spin $I = 14\hbar$ and $E_x \lesssim 11$ MeV. Hence, in the range $E_x \sim 5$–9 MeV the γ-ray flux amongst positive-parity states becomes more and more fragmented and rather irregular (ND5). Apart from the 1774-keV, $8^+ \rightarrow 6^+$ transition, the relative yield of all such γ rays is on the level of 1% or less. Here, the 4231-keV, 5^+ state in ND5 is a good example for a definite assignment of spin and parity, despite the lack of angular correlation data of both feeding or depopulating transitions; the fact that only a stretched $E2$ 1670-2072-1846-keV γ-ray cascade can connect the known 7976 keV, 9^+ (ND6) and 2385 keV, 3^+ (ND2) levels ensures the 5^+ label of the 4231-keV state.
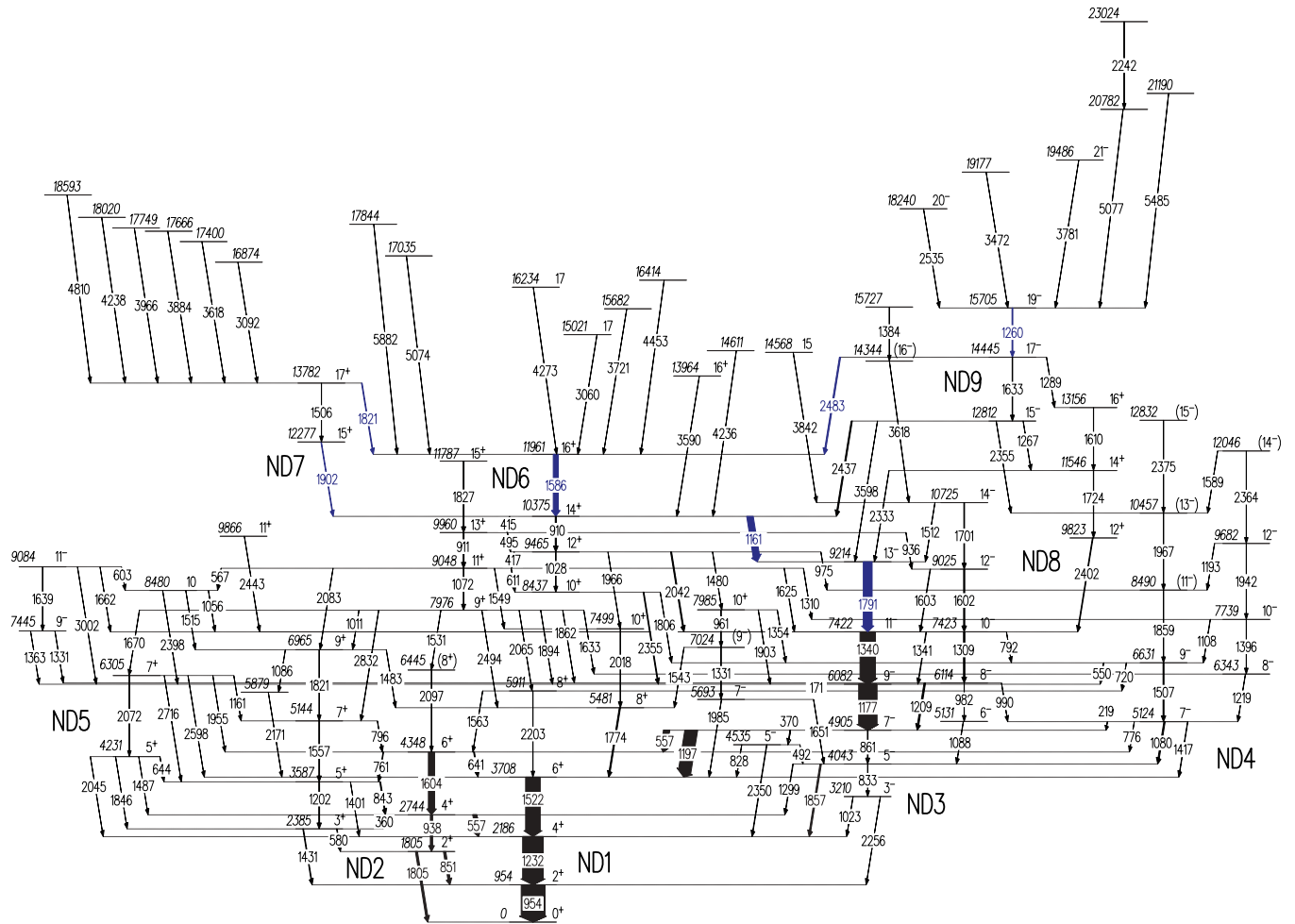
FIG. 2. (Color online) Normally deformed region of the proposed level scheme of ^{62}Zn. Energy labels are in keV. See text for details.

The structures ND1, ND2, ND3, and ND5 are connected with the somewhat more regular positive-parity sequence ND6, which terminates in the yrast 11 787-keV, 15^+ (newly observed) and 11 961-keV, 16^+ levels. The latter decays via the 1586-1161-keV, $E2$-$E1$ cascade towards the 9214-keV, 13^- yrast state of ND3. These two γ rays mark the end of transitions with relative intensities in excess of 10%. Thus, in particular, the 1586-keV $E2$ line is a valuable source for assessing DCO ratios of many of the weak connections (cf. Figs. 1 and 2) towards the rotational bands.

Next to ND6, the previously unobserved three γ-ray transitions at 1506, 1821, and 1902 keV lead to the yrast 17^+ state at 13 782 keV, which terminates this ND7 sequence. The DCO ratios of both the 1821- and the 1902-keV lines clearly point at mixed $E2/M1$ character, while the number available for the 1506-keV transition is consistent with a stretched $E2$ assignment. It is also interesting to note that the $\delta(E2/M1)$ mixing ratios for the 1821- and 1902-keV transitions are very similar; either moderate ($\delta \approx 0.3$) or significant ($\delta \approx 2.0$) quadrupole mixture is seen. Similar to the 11 961-keV, 16^+ state, the 13 782-keV level is also fed by several 3- to 5-MeV high-energy γ-ray transitions.

The newly identified structure ND4 consists of two signature partner sequences of negative parity. At the bottom,

ND4 is energetically located 200–300 keV above the yrast negative-parity cascade ND3. The larger level spacing of ND4 compared to ND3 leads to an increasing yrare character, manifesting in quickly decreasing yields of the transitions found to belong to ND4. The 7^- spin-parity assignment to the band head of ND4 is suggested by the stretched $E2$ character of the 1080-keV connection to the 4043-keV 5^- state of ND3 and the $\Delta I = 1$ type of the 1417-keV decay into the yrast 6^+ level at 3708 keV (ND1). With the help of the distinct mixed $\Delta I = 1$ character of the 1219-keV transition [$R_{\rm DCO} = 0.31(3), \delta \approx 0.2$ or $\delta \approx 2.0$], the 8^- assignment of the 6343-keV level can be easily established. The spin-parity assignments along the band follow the derived DCO ratios and are based the rotational-like behavior towards the top of ND4.

Several γ-ray cascades lead to the yrast 19^- state at 15 705 keV, which is considered as a part of the structure labeled ND9. The 1260-1633-2437-keV and 1260-2483-1586-keV branches into the yrast 14^+ state at 10 375 keV are in accordance with Ref. [20], while the decay paths via the positive-parity states at 13 156, 11 546, and 9823 keV into the yrast 11^- level at 7422 keV are newly established and form a sequence labeled ND8. The DCO ratios of the 2402-keV, $12^+ \rightarrow 11^-$ and 1267-keV, $15^- \rightarrow 14^+$ transitions are in agreement with stretched dipole transitions. The connections of ND8 and ND9 to various other

structures of the complete level scheme (cf. Fig. 1) constrain the parities of the concerned states; for example, the plain existence of the 3598-keV $E2$ branch from the 12 812-keV state calls for its negative-parity assignment.

B. The terminating bands TB1 and TB2

TB1 and TB2 are previously known [20] terminating bands. The present results are consistent with the earlier data, but contain some additional information [41].

In brief, structure TB1 comprises two bands TB1a and TB1b, which are signature partners. The bands consist of about equally intense $E2$ transitions and connecting $E2/M1$ transitions, on the level of some 5% relative yield. The latter all have noticable mixing ratios on the level of $\delta(E2/M1) \sim$ −0.1–0.2 (cf. Table I). In Ref. [20], positive parity was tentatively assigned to the states in TB1. Current results confirm the parity of TB1a and TB1b by several linking transitions, which are connected to the established low-spin region. The fact that the spin $I = 12\hbar$ 10 631-keV state decays into established 10^+, 11^+, and 11^- states in the ND regime leaves, in conjunction with the DCO ratios of some of the corresponding transitions, only room for a positive-parity assignment. Similarly, the extended decay pattern of the 13^+, 11 178-keV level supports this assignment. The maximum spin of TB1 is $I^\pi = 21^+\hbar$ at $E_x = 19.5$ MeV for structure TB1a (signature $\alpha = 1$) and $I^\pi = 20^+\hbar$ at $E_x = 17.6$ MeV for structure TB1b (signature $\alpha = 0$).

Structure TB2 consists also of two signature partner bands with about equally intense $E2$ transitions inside each signature band and $E2/M1$ transitions between them. Similar to TB1, the relative yield of transitions is on average some 5%, not least because TB2 turns out to be yrast in the spin range $I \sim 20\hbar$–$23\hbar$. Previously unobserved weak transitions connect TB2 with TB1, and in line with the arguments given above, the complex decay pattern of primarily the $I = 14$ 12 329-keV and $I = 15$ 12 993-keV states, combined with DCO ratios of some of the corresponding transitions, leads to a definite negative-parity assignment of TB2 [41]. This assignment is underpinned with the 969-719-914 bypass between TB2 and ND9 as well as the relatively intense 1928-keV $E2$ transition connecting the 16 373-keV level in TB2 with the 14 445-keV level associated with ND9.

The spin ranges up to $I^\pi = 23^-\hbar$ at $E_x = 21.0$ MeV for structure TB2a (signature $\alpha = 1$) and $I^\pi = 24^-\hbar$ at $E_x = 23.2$ MeV for structure TB2b (signature $\alpha = 0$). In addition, there are some 15 isolated states observed which, though seemingly not giving rise to any bandlike structure, decay into TB2 via high-energy γ-ray transitions in the range $E_\gamma \sim 3.4$–5.3 MeV.

C. The band WD1

This band was introduced in Ref. [18]. Even spins and positive parity have been established, with the band covering a spin range of $I = 16\hbar$–$30\hbar$ and an energy range of $E_x \sim 15$–34 MeV. Below the 20^+ 18 677-keV level, the band forks into several branches and connects mainly towards the 16^+ yrast
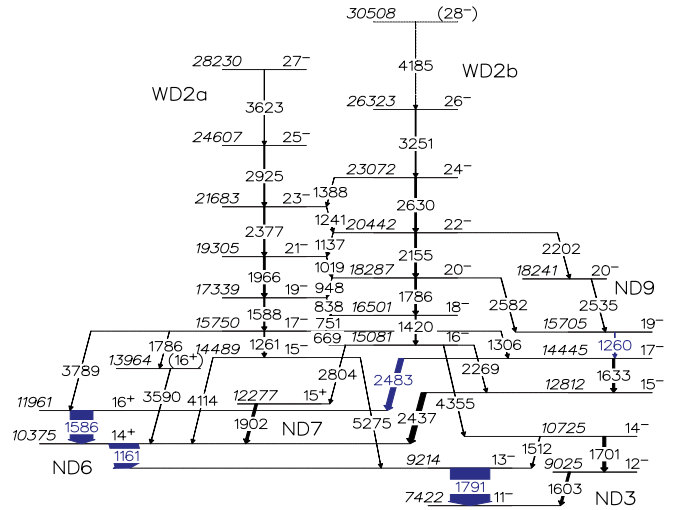
FIG. 3. (Color online) Decay scheme of band WD2 of the level scheme of ^{62}Zn. Energy labels are in keV and tentative levels and transitions are dashed. The widths of the arrows correspond to the relative intensities of the γ rays. Relevant transitions of the ND scheme are marked in blue.

state at 11 961 keV (ND6). Here, an additional two-step link towards the 20^+ 18 677-keV level in WD1 is established via a 4509- to 2207-keV cascade.

D. The band WD2

WD2 is the only well-deformed coupled band in the decay scheme of ^{62}Zn. It consists of two signature partner sequences illustrated in Fig. 3. The signature $\alpha = 1$ sequence (WD2a) on the left-hand side of Fig. 3 covers the spin range $I = 15\hbar$–$27\hbar$, and the signature $\alpha = 0$ sequence (WD2b) $I = 16\hbar$–$28\hbar$, lying roughly between 15 and 30 MeV excitation energy. The topmost transition in WD2b at 4185 keV is very weak and only tentatively place based on the analysis of the $\gamma\gamma\gamma$ cube.

The relative yields of the in-band quadrupole transitions amount to some 1%–2%, while the interlinking dipole transitions are about one order of magnitude less intense. The former are observed with good statistics in the spectra displayed in Figs. 4(a) (WD2a) and 4(b) (WD2b). The most intense dipole connection at 838 keV is highlighted in the inset of Fig. 4(b), which is a γ-ray spectrum in coincidence with the low-lying $E2$ transitions in WD2b (1420 or 1786 keV) and the high-lying $E2$ transitions in WD2a (1966, 2377, or 2925 keV). The $21^- \rightarrow 20^-$ connection at 1018 keV is also weakly seen. Indirect evidence for the dipole connections are the weak but visible peaks at energies corresponding to quadrupole transitions of WD2b in the spectrum focusing on WD2a and vice versa. These are marked with stars in Fig. 4.

WD2 is linked into several parts of the medium-spin level scheme of ^{62}Zn: Connections are observed to ND3, ND6, ND7, ND9, as well as a 2519-keV transition between the 15 750-keV state in WD2a and the 13 231-keV state in TB1 (not included in Fig. 3 for clarity). Starting with WD2a, a rather intense transition at 3789 keV connects the 15 750-keV state with the yrast 16^+ state at 11 961 keV. The DCO ratio
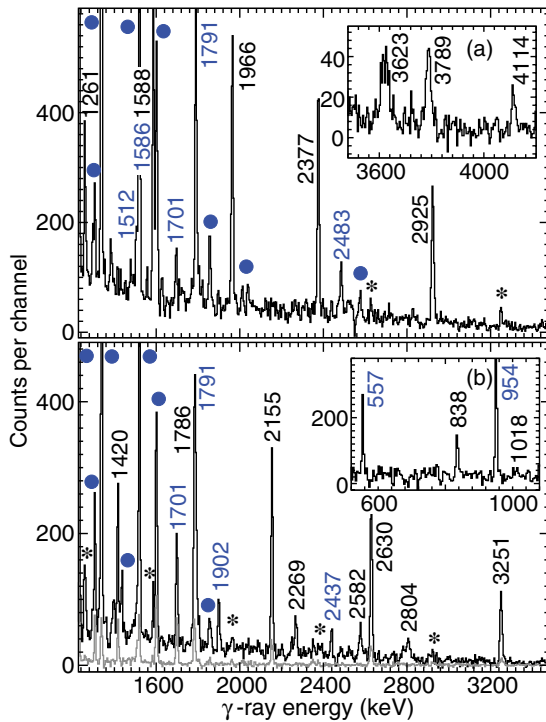
FIG. 4. (Color online) Set of γ-ray spectra related to band WD2. (a) Sum of γ-ray spectra in coincidence with any combination of one of the 1261-, 1588-, and 1966-keV transitions and one of the 1261-, 1588-, 1966-, 2377-, 2925-, and 3623-keV transitions placed in WD2a. The inset shows the high-energy part of the spectrum. (b) WD2b is displayed by the sum of γ-ray spectra in coincidence with any combination of one of the 1420-, 1786-, 2155-, and 2630-keV transitions and one of the 1420-, 1786-, 2155-, 2630-, and 3251-keV transitions with the spectrum in black. The gray spectrum is in coincidence with one of these four band members and the 4355-keV decay-out transition. The inset shows the low-energy part of a spectrum in coincidence with the 1420- or 1786-keV transitions belonging to WD2b and the 1966-, 2377-, or 2925-keV transitions placed in WD2a. Energy labels are in keV, and blue labels or solid circles indicate transitions belonging to the ND part of the ^{62}Zn level scheme. The peaks marked with stars indicate quadrupole transitions of WD2b in panel (a) and WD2a in panel (b). The binning is 4 keV per channel for all spectra.

of this transition points at dipole character; that is, the level at 15 750 keV has spin $I = 17\hbar$, likewise the weaker 4114-keV connection between the yrast 10 375-keV 14^+ state of ND6 and the 14 489-keV state in WD2a. Because this state also decays via a 5275-keV γ line into the yrast 13^- level at 9214 keV (ND3), the negative parity assignment to WD2 becomes mandatory. Furthermore, the $E2$ character of the relatively intense 4355-keV link between the lowest state in WD2b and the 10 725-keV 14^- level in ND3 confirms the negative-parity assignment.

Coincidences with the 4355-keV transition and any of the four lower members of WD2b are illustrated by the gray spectrum in Fig. 4(b). The WD2b quadrupole transitions up to the 3251-keV line are visible with decreasing yield. In particular, a peak at 1701 keV is clearly observed, which corresponds to the $14^- \rightarrow 12^-$ transition in ND3. Together

with a similarly clean spectrum of the above-mentioned 3789-keV link, both energetic positioning and spin-parity assignments of WD2 are simple. Moreover, the parallel 2804- to 1902-keV and 2289- to 2437-keV sequences connect the 15 081-keV level in WD2b with the 10 375-keV yrast state via levels associated with ND7 and ND9, respectively. The corresponding peaks are clearly seen in Fig. 4(b). Similarly, 2582- and 2202-keV transitions form $E2$ connections between WD2b and ND9.

E. The band WD3

Figures 5 and 6 show the results of band WD3. A sequence of six $E2$ transitions at 1580 (tentative), 1825, 2192, 2594, 3039, and 3830 keV is observed on top of the 13 497-keV state. The relative yield of the central part of WD3 amounts to about 1%. The main and rather intense link at 3116 keV (cf. Fig. 6) connects the 17^- level in WD3 with the 11 961-keV 16^+ state in ND6. The value $R_{\rm DCO}(3116) = 0.67(7)$ is a clear sign of a $\Delta I = 1$ transition, and owing to the 2265- and 2456-keV connections into structure ND9, the 3116-keV line must be a parity-changing $E1$ transition; that is, WD3 has negative parity. The DCO ratios along the band are consistent with $E2$ character, while the spin-parity assignments of both the lowest and the topmost levels in WD3 are tentatively assigned based on the presumed rotational character.

The spectrum in Fig. 6(a) shows a sum of spectra in coincidence with any combination of the transitions at 1825, 2192, 2594, and 3038 keV. The inset shows an apparent 3830-keV line placed on top of WD3, while a closer inspection reveals a shoulder on the left-hand side of the intense 1586-keV peak (ND6), which is absent in comparable spectra of other well-deformed bands. The $\gamma\gamma\gamma$ analysis gives additional evidence for a tentative line at 1580 keV at the bottom of
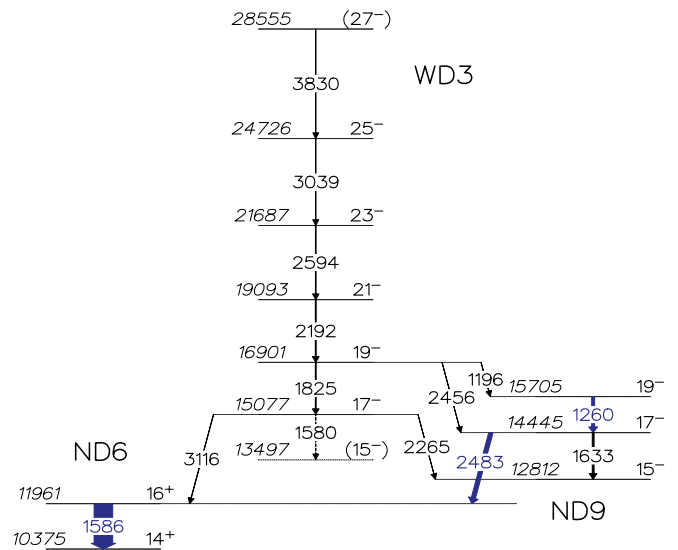

FIG. 5. (Color online) Decay scheme of band WD3 of the level scheme of ^{62}Zn. Energy labels are in keV and tentative levels and transitions are dashed. The widths of the arrows correspond to the relative intensities of the γ rays. Relevant transitions of the ND scheme are marked in blue.
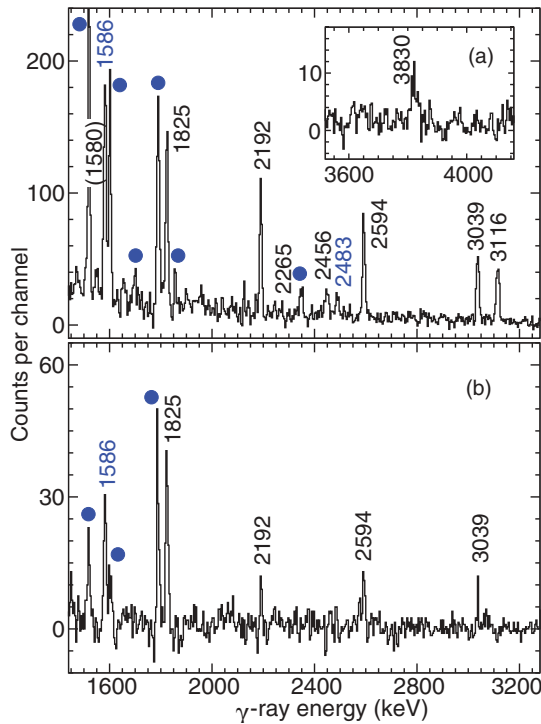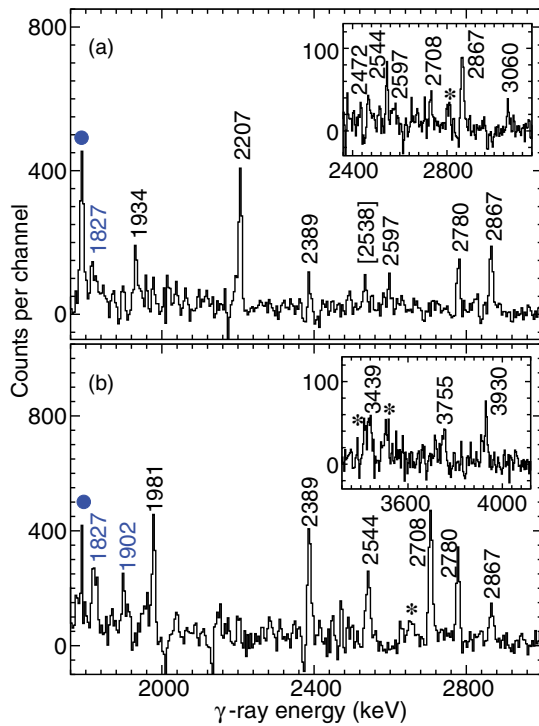
FIG. 6. (Color online) γ-ray spectra related to band WD3. (a) The spectrum is in coincidence with any combination of two of the four main members of the band at 1825, 2192, 2594, and 3039 keV. The inset shows the high-energy part of the spectrum. (b) The spectrum is in coincidence with the 3116-keV linking transition and any of the three band members at 2192, 2594, and 3039 keV. Energy labels are in keV, and blue labels or solid circles indicate transitions belonging to the ND part of the ^{62}Zn level scheme. The binning is 4 keV per channel.

WD3. Next to other transitions in the normally deformed region of the level scheme of ^{62}Zn (solid circles), the transitions at 2456, 2483, and 3116 keV can be seen, which determine the placement of WD3. The latter is highlighted in Fig. 6(b), which is a spectrum in coincidence with the 3116-keV linking transition and any of the three band members at 2192, 2594, and 3039 keV. The 1825-keV in-band member as well as the 1586-keV are marked and define the decay path.

F. The bands WD4 and WD5

Structure WD4 is illustrated in Figs. 7 and 8. It is formed by a set of γ rays starting from the 19^+ level at 18 516 keV merging into the 27^+ level at 28 205 keV denoted WD5. WD4 decays into the 17^+ state at 13 782 keV (ND7) via the 4734-keV linking transition. The DCO-ratio of the latter, $R_{\mathrm{DCO}}(4734) = 1.20(25)$, in combination with yrast considerations and the 3060-keV connection towards WD5 defines the spin and parity assignment of the 18 516-keV state. Thereafter, the DCO ratios are available and consistent with $E2$ character along WD4 except for the topmost, tentative 3060-keV line.

The γ-ray spectrum in Fig. 8 is taken in coincidence with the 4734-keV decay-out transition of WD4. The three band
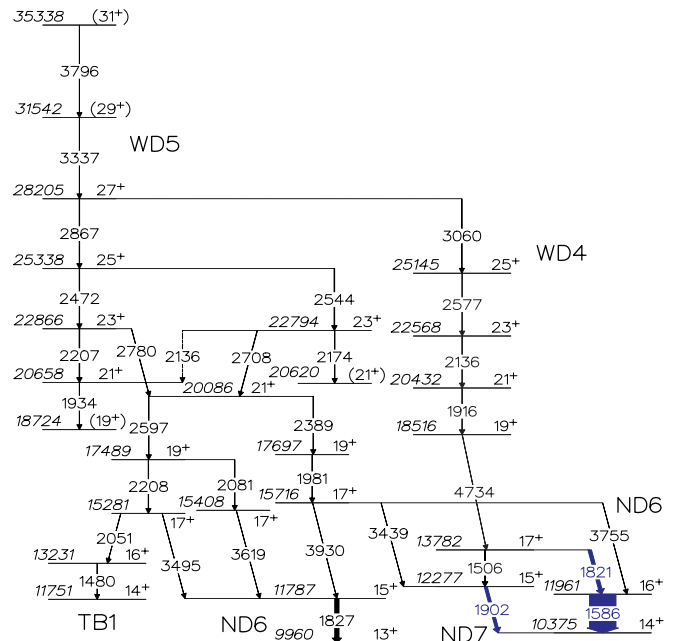
FIG. 7. (Color online) Decay scheme of WD4 and WD5 of the level scheme of ^{62}Zn. Energy labels are in keV and tentative levels and transitions are dashed. The widths of the arrows correspond to the relative intensities of the γ rays. Relevant transitions of the ND scheme are marked in blue.

members at 1916, 2136, and 2577 keV are clearly seen, as well as the transitions at 1506, 1586, 1821, and 1902 keV, which define the decay paths of the 13 782-keV state of ND7. The blue circles mark transitions further down in the ND yrast decay scheme of ^{62}Zn. Note that the band has a relative yield of about 0.4% and the high-energy link only 0.13%. Nevertheless, Fig. 8 unambiguously determines the WD4 decay path shown in Fig. 7. The 4734-keV link is highlighted in the inset of
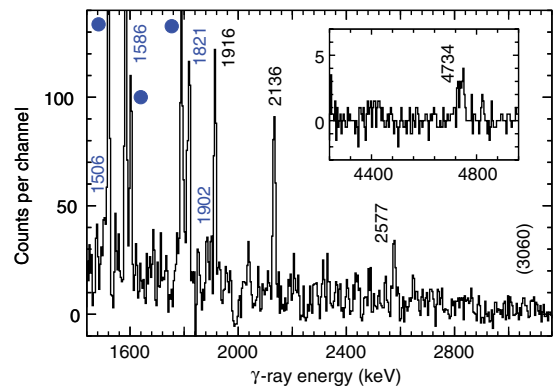
FIG. 8. (Color online) γ-ray spectra related to band WD4. The main is in coincidence with the 4734-keV decay-out transition. The inset shows the relevant high-energy part of another spectrum, which is in coincidence with either one of three WD4 members at 1916, 2136, or 2577 keV and the 1821-keV transition (ND7). Energy labels are in keV, and blue labels or solid circles indicate transitions belonging to the ND part of the ^{62}Zn level scheme. The binning is 4 keV per channel.

FIG. 9. (Color online) Set of γ-ray spectra related to band WD5. (a) γ-ray spectrum in coincidence with the 2472-keV transition. The inset shows the relevant high-energy part of a spectrum in coincidence with the 3337-keV line. (b) γ-ray spectrum in coincidence with the 1981- or 2389-keV transitions. The inset shows the high-energy part of this spectrum. Energy labels are in keV. Blue labels or solid circles indicate transitions belonging to the ND part of the ^{62}Zn level scheme. Stars or energy labels in square brackets mark contaminations or weak transitions not placed in the level scheme, respectively. The binning is 4 keV per channel.

Fig. 8, which is a spectrum in coincidence with one of the three WD4 members and the 1821-keV transition from ND7.

Based on Fig. 8 and additional studies with the $\gamma\gamma\gamma$ cube a transition at 3060 keV could be added tentatively on top of WD4, reaching a level at 28 205 keV, which is a member of WD5. In fact, the 3337-keV transition of WD5 provides coincidences with both the 3060-keV line of interest and, of course, the lower members of WD5, in particular the 2867-keV transition. This is shown in the inset of Fig. 9(a). Hence, WD4 and WD5 are connected at spin $I = 27\hbar$.

Similar to WD4, WD5 is found to comprise only signature $\alpha = 1$ positive-parity states. However, WD5 reveals itself as a rather complex structure, mainly composed of a cascade of six quadrupole transitions at 1934, 2207, 2472, 2867, 3337, and 3796 keV, drawn on the left-hand side of Fig. 7. Note that the topmost transition at 3796 keV is only observed in data set 2. This cascade, illustrated by the γ-ray spectrum in coincidence with the 2472-keV member in Fig. 9(a), covers spins $I = 19\hbar$–$31\hbar$ and excitation energies up to 35 MeV. The 2207-2472-keV sequence is paralleled by the 2136-2544 cascade, with a 2174-keV transition depopulating the 23^+, 22 794-keV state fed by the 2544-keV line. The depopulation of neither the (19^+), 18 724- nor the (21^+), 20 620-keV

level could be defined owing to insufficient statistics or contaminating transitions from other bands in ^{62}Zn. Note that the average sum of relatively yields across WD5 is about 0.8%–1.0%, whereas the relative intensities of all individual transitions associated with WD5 are less than 0.5%.

Both 23^+ states of WD5 are directly connected with the 21^+ level at 20 086 keV. The decay of this rather low-lying 21^+ level forks first into two 19^+ and subsequently three 17^+ states. On of these branches and its coincidences with the high-lying transitions of WD5 is illustrated by the γ-ray spectrum in Fig. 9(b), which is in coincidence with the 1981- or 2389-keV transitions. The decay-out region of the three 17^+ states provides a number of linking transitions, mainly into structures ND6 and ND7 [cf. 1827- and 1902-keV lines in Fig. 9(b)] but also into TB1 via a line at 2051 keV. The DCO ratio of this transition, which clearly points towards dipole character, and the one of the 3495-keV link into the 15^+, 11 787-keV level of ND6 determines the spin and parity of the 15 281-keV state. This is consistent with all six linking transitions decaying into either 15^+ or 16^+ states of the ND part of the level scheme as well as the above-mentioned 3060-keV $E2$ connection between WD4 and WD5. Within WD5, most of the spins and parities of the states are assigned based on DCO ratios of the most intense transitions (see Table I). Last but not least, the inset of Fig. 9(b) shows the 3439-, 3755-, and 3930-keV transitions attributed to the decay-out of the 15 716-keV state.

G. The bands WD6 and WD7

WD6 is shown on the left-hand side of Fig. 10. It is connected to WD7 drawn on the right-hand side of the figure. WD6 and WD7 have relative yields of about 0.5% each. Both bands have signature $\alpha = 1$ and are found to carry negative parities. Hence, they interact at their closest approach in energy at around spin $I = 21\hbar$.
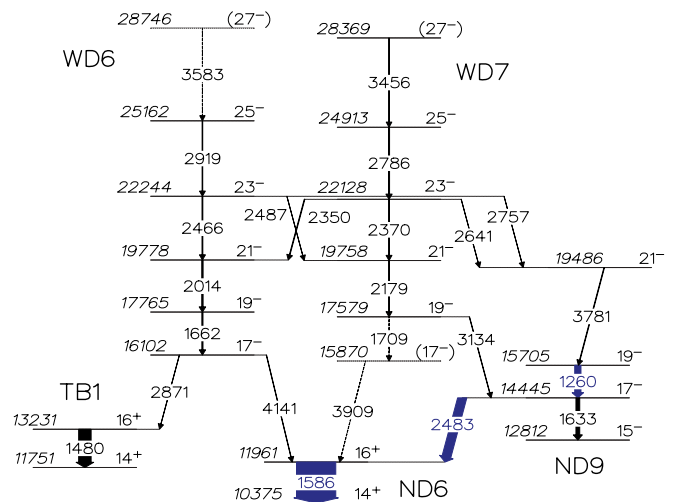

FIG. 10. (Color online) Decay scheme of bands WD6 and WD7 of the level scheme of ^{62}Zn. Energy labels are in keV and tentative levels and transitions are dashed. The widths of the arrows correspond to the relative intensities of the γ rays. Relevant transitions of the ND scheme are marked in blue.
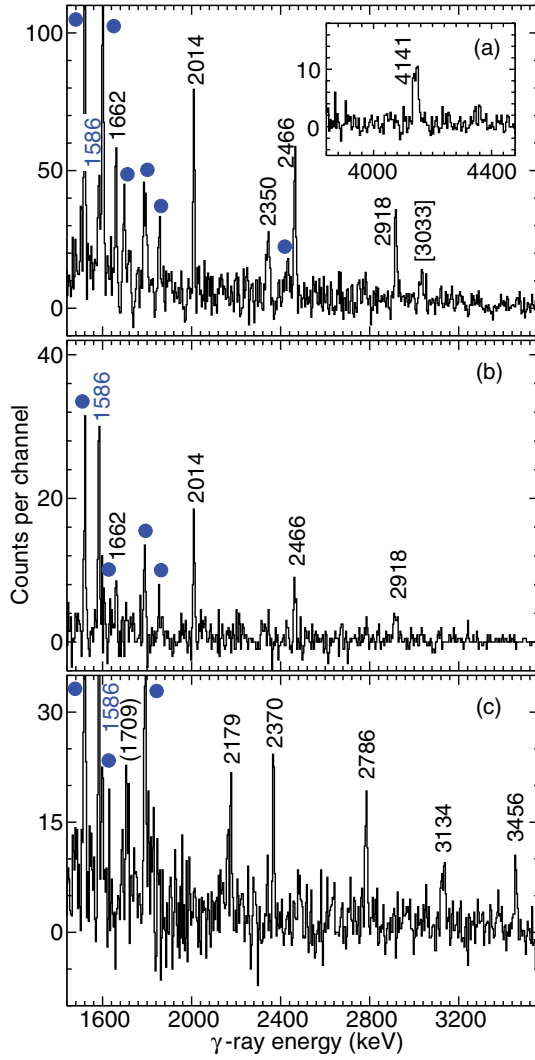
DCO ratio—as well as the weak side branch via the 19 486-keV state into established states of ND9 (cf. Fig. 10): Based on the 4141-keV link, the observed bottom state in WD6 has spin $I = 17$. Based on the well-established DCO ratios of the 1662-, 2014-, and 2350-keV lines, the 22 128-keV state in WD7 has spin $I = 23$. This state decays via the 2641- to 3781-keV cascade into the known $I^\pi = 19^-$ state of ND9, or via the 2370-2179-3134-keV sequence into the known $I^\pi = 17^-$ state of ND9. Thus, all these transitions must have stretched $E2$ character (cf. Sec. II), and both bands WD6 and WD7 are composed of negative-parity states.

The spectrum in Fig. 11(a) comprises also the connecting line towards WD7 at 2350 keV and, somewhat less pronounced, the 2786-keV member of WD7. The 3033-keV peak in Fig. 11(a) is set in square brackets; most likely it is a decay-out transition from the 16 102-keV level of WD6. Its width is comparable to the 3134-keV peak in Fig. 11(c). However, owing to lack of statistics it was not possible to make a firm placement in the level scheme. The 2871-keV link into TB1 is very weak.

Figure 11(c) is the γ-ray spectrum illustrating WD7. It is the sum of coincidences with two of the three central transitions at 2179, 2370, and 2786 keV. Despite the fact that the 1709-keV peak in Fig. 11(c) is apparent, it is not possible to firmly establish its placement at the bottom of WD7. It carries about half of the yield of the 3134-keV linking transition, the DCO ratio of which is consistent with the spin and parity assignments of the states in WD6 and WD7 (see above).

H. Bands WD8 and WD9

Figure 12 illustrates the details of the decay pattern of bands WD8 and WD9. Both of them are linked into the ND6 yrast 16^+ state at 11 961 keV. The weak 5685-keV linking transition
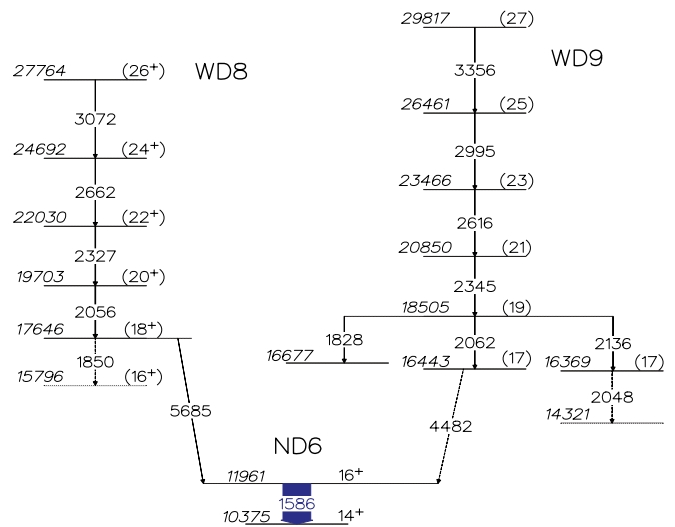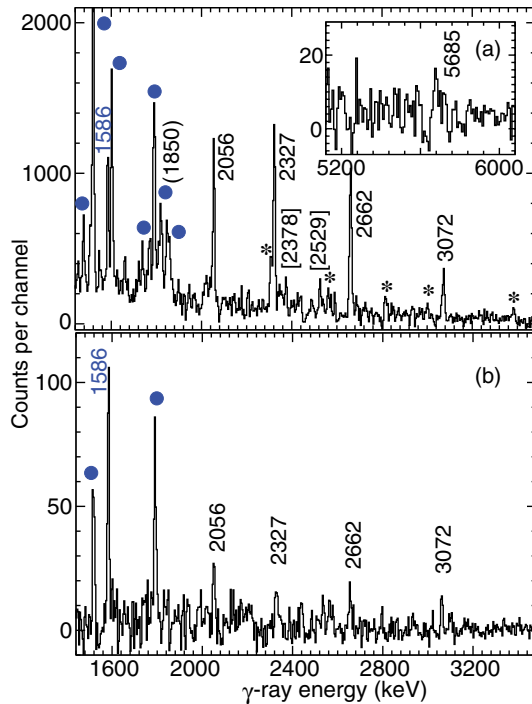
FIG. 11. (Color online) Set of γ-ray spectra related to bands WD6 and WD7. (a) γ-ray spectrum in coincidence with any combination of two of the four main members of the band WD6 at 1662, 2014, 2466, and 2918 keV. The inset shows the high-energy part of the spectrum. (b) Spectrum in coincidence with one of these four band members and the 4141-keV linking transition. (c) γ-ray spectrum in coincidence with any combination of two of the three main members of the band WD7 at 2179, 2370, and 2786 keV. Energy labels are in keV, and blue labels or solid circles indicate transitions belonging to the ND part of the ^{62}Zn level scheme. The binning is 4 keV per channel.

WD6 consists of a total of four well-defined $E2$ transitions at 1662, 2014, 2466, and 2918 keV [see Fig. 11(a)]. The topmost transition at 3583 is tentatively suggested. On the contrary, the 4141-keV linking transition is clearly seen in the inset of Fig. 11(a), and its DCO ratio $R_{\mathrm{DCO}}(4141) = 0.51(10)$ is decisive for the spin assignment of both WD6 and WD7. The firm placement of the 4141-keV line between the 11 961-keV 16^+ state of ND6 and the bottom state of WD6 at 16 102 keV is ensured by the spectrum in Fig. 11(b), which is in coincidence with any of the four main WD6 members and the 4141-keV line. Note that the parity of the structure is simply defined by the existence of the 3134-keV transition—supported by its

FIG. 12. (Color online) Decay scheme of bands WD8 and WD9 of the level scheme of ^{62}Zn. Energy labels are in keV and tentative levels and transitions are dashed. The widths of the arrows correspond to the relative intensities of the γ rays. Relevant transitions of the ND scheme are marked in blue.

FIG. 13. (Color online) γ-ray spectra related to band WD8. (a) The spectrum is in coincidence with the 2056-, 2327-, 2662-, and 3072-keV transitions. The inset shows the high-energy part of the spectrum. (b) The spectrum is in coincidence with the 5685-keV linking transition. Energy labels are in keV, and blue labels or solid circles indicate transitions belonging to the ND part of the ^{62}Zn level scheme. Stars mark small contaminating peaks arising from the 2058-keV line of SD2. The binning is 4 keV per channel for the main spectrum but 8 keV per channel for the inset.

of WD8 is shown in the inset of Fig. 13(a). A coincidence spectrum of this transition is presented in Fig. 13(b), with its positioning in the level scheme being further evidenced in the triples analysis. Specifically, a spectrum in coincidence with both this linking transition and any of the intense γ-ray lines in ND1 and ND3 reveals not only the 1586-keV transition of ND6 but also the 2056- and 2327-keV transitions associated with WD8. The band itself is shown in the main spectrum of Fig. 13(a) and present in Fig. 13(b) with the exception of the tentative in-band 1850-keV transition.

WD8 has about 0.4% relative yield and reaches up to an excitation energy of 28 MeV. Once more, the presence of the 1586-keV line as well as the absence of higher-lying transitions of the ND scheme of ^{62}Zn at, for example, 2437 or 2483 keV, is obvious. The stars in Fig. 13(a) mark contaminating transitions arising from the 2058-keV line in SD2. The evidence for the 1850-keV line is rather weak owing to interference with the 1857-keV $5^- \rightarrow 4^+$ transition. Small peaks at 2378 and 2529 keV can be seen in the spectrum of Fig. 13 as well. Lack of statistics prevents any firm conclusion on how and where they could be connected to WD8. A tentative spin and parity assignment is suggested based on the high transition energy and yrast arguments. DCO ratios derived for the 2056-, 2327-, and 2662-keV transitions account for $E2$ character of these band members.
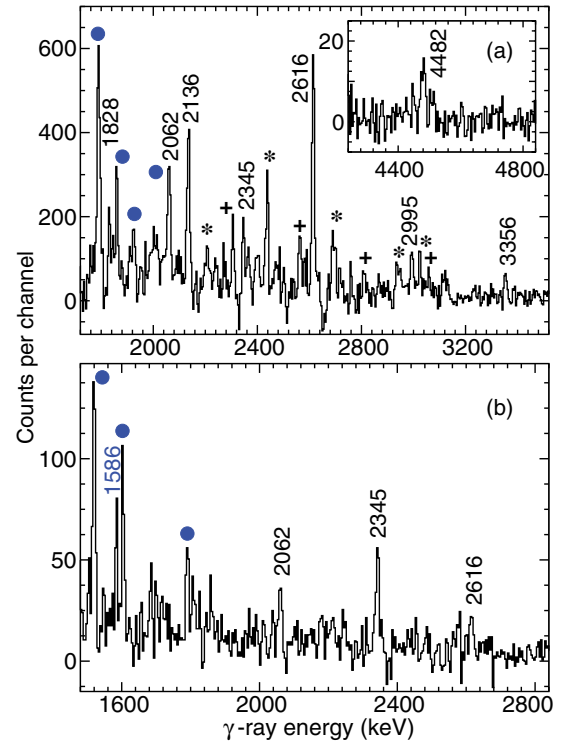
FIG. 14. (Color online) γ-ray spectra related to band WD9. (a) Spectrum in coincidence with the 2345- and 2995-keV transitions. The inset shows the high-energy part of the spectrum. (b) Spectrum in coincidence with the 4482-keV decay-out transition. Energy labels are in keV, and blue labels or solid circles indicate transitions belonging to the ND part of the ^{62}Zn level scheme. Stars mark contaminating peaks arising from unresolved coincidences of a line at 2341 keV with transitions belonging to SD1. Plus signs mark minor peaks arising from the 2994- and 3001-keV decay-out lines of SD2. The binning is 4 keV per channel.

In case of WD9 it is difficult to provide clean coincidence spectrum with sufficient statistics: The main band members at 2345 and 2616 keV have only 0.3% relative yield. The spectrum displayed in Fig. 14(a) is taken in coincidence with the 2345- and 2995-keV members of WD9. Along the band, peaks at 1828, 2062, 2136, and 2616 keV are evident, and a weak line at 3356 keV is also apparent. Weak contaminating peaks are present in the spectrum arising from an unresolved doublet structure at 2341 keV (SD1) and decay-out transitions at some 3 MeV associated with SD2. The 4482-keV decay-out transition of WD9 is highlighted in the inset of Fig. 14(a), and Fig. 14(b) provides the spectrum in coincidence with the 4482-keV line. Similar to the discussion on WD8 above, this line can be confirmed to belong to WD9 in more detailed steps of the coincidence analysis. However, its placement—and hence the position of WD9 in energy—can only be made tentative, as statistics are low and because a number of doublets are distorting, in particular the rather intense 2064-keV transition in TB2. The 4482-keV link is also too weak to provide a DCO ratio. Its dipole character is proposed owing to WD9 intensity-related yrast arguments, and this leads to the tentative assignment of odd spin values for the band itself up to a spin $I = 27\hbar$ level at about 30 MeV
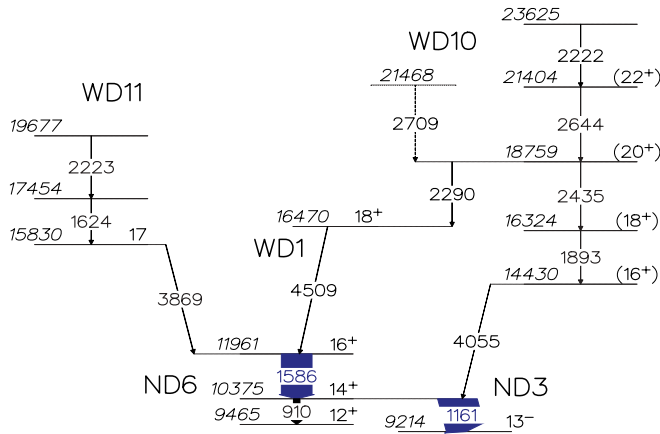
FIG. 15. (Color online) Decay scheme of bands WD10 and WD11 of the level scheme of ^{62}Zn. Energy labels are in keV and tentative levels and transitions are dashed. The widths of the arrows correspond to the relative intensities of the γ rays. Relevant transitions of the ND scheme are marked in blue.

excitation energy. Altogether, WD9 marks the experimentally least defined rotational structure in the level scheme.

I. Bands WD10 and WD11

The relatively short sequences WD10 and WD11 are shown in Fig. 15. WD10 comprises as a basis the transitions at 1893, 2435, and 2644 keV, which are connected to the 10 375-keV 14^+ yrast state (ND6). Despite minor contaminations with doublet transitions at 1891 and 1894 keV, the spectrum in Fig. 16(a) evidences WD10. The spectrum in coincidence with the 1893-keV line provides a clean and rather intense peak at 4055 keV, the DCO ratio of which is consistent with stretched $E2$ character. This tentatively implies that WD10 has even spins and positive parity. The 2435- and 2644-keV transitions are also visible in Fig. 16(a) with decreasing yield. A $\gamma\gamma\gamma$ analysis involving transitions from the ND part of the level scheme in conjunction with the relatively intense 4055-keV link provides evidence for the lines at 2222 keV and, tentatively, 2709 keV. Both are also weakly present in Fig. 16(a). Furthermore, a γ-ray transition at 2290 keV is found in coincidence with the 2644-keV line. It decays to the 18^+ state at 16 489 keV—thus supporting the spin-parity suggestion of WD10—because the 18^+ state is associated with WD1 and decays further to the 16^+ 11 961-keV yrast level. The most intense transitions of WD10 have only some 0.2% relative yield. Thus, no further transitions or connections to other bands could be derived.

WD11 is illustrated in Fig. 16(b). The spectrum taken in coincidence with the 3869-keV link into the 16^+ yrast state of ND6 provides the relevant peaks at 910, 1161, and 1586 keV as well as the two band members at 1624 and 2223 keV, respectively. The transition belonging to the weak peak at 2538 keV may feed into the lowest level of WD11 at 15 830 keV, because it is neither coincident with the 1624- nor the 2223-keV transition. The DCO ratio of the 3869-keV line is clearly consistent with stretched dipole character. Hence, the 15 830-keV state of WD11 has spin $I = 17\hbar$. The low yield of the
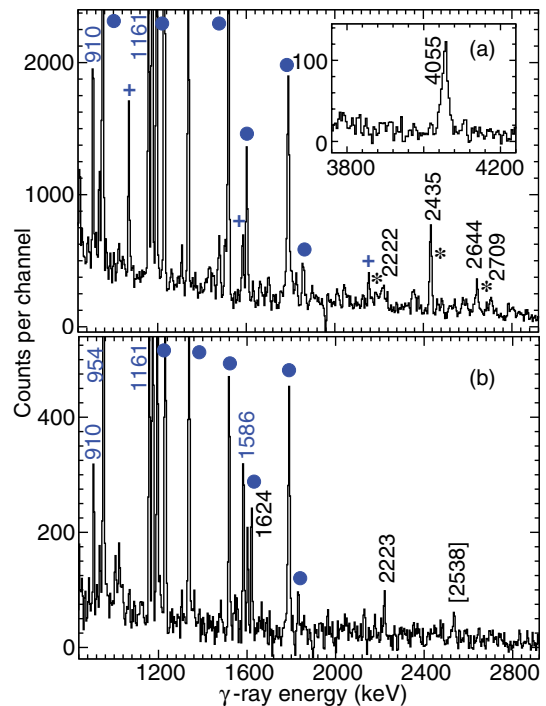

FIG. 16. (Color online) Set of γ-ray spectra related to bands WD10 and WD11. (a) γ-ray spectrum in coincidence with the 1893-keV transition of WD10. The inset shows the high-energy part of the spectrum. Blue plus signs mark contaminating peaks arising from a 1894-keV transition connecting the 9^+ state (ND6) with the 9^- level at 6082-keV (ND3). Stars mark small contaminating peaks arising from coincidences with the 1891-keV transition placed in the decay-out regime of SD1. (b) γ-ray spectrum in coincidence with the 3869-keV transition linking WD11 into the 16^+ yrast state (ND6). Energy labels are always in keV, and blue labels or solid circles indicate transitions belonging to the ND part of the ^{62}Zn level scheme. The binning is 4 keV per channel.

band members or contaminating lines from other parts of the ^{62}Zn level scheme prevent any DCO-ratio measurements of the in-band transitions of WD10 and WD11.

J. The superdeformed bands SD1, SD2, and SD3

Apart from some minor adjustments of transition energies and intensities and in parts a few more transitions in the respective decay-out regime, the presentation of the superdeformed bands SD1, SD2, and SD3 is in accordance with Figs. 1–3 in Ref. [18]. SD1 is assigned negative parity, covers a spin range of $18\hbar$–$34\hbar$, and reaches a maximum excitation energy in excess of 40 MeV. A comparatively extensive decay-out regime is established, and at the very top a forking is observed, that is, two parallel transitions of 3958 keV [18] and 4234 keV. SD2 is considered the $\alpha = 1$ signature partner of SD1 [18], involves a record-high discrete-energy state at 42.5 MeV excitation energy, and lies amongst the fastest rotating nuclei. SD2 is found to interact with a new, parallel sequence SD5 (see below). SD3 has signature $\alpha = 0$, positive parity, and spin values $I = 16$–30 and remains unchanged with respect to the previous publication [18].
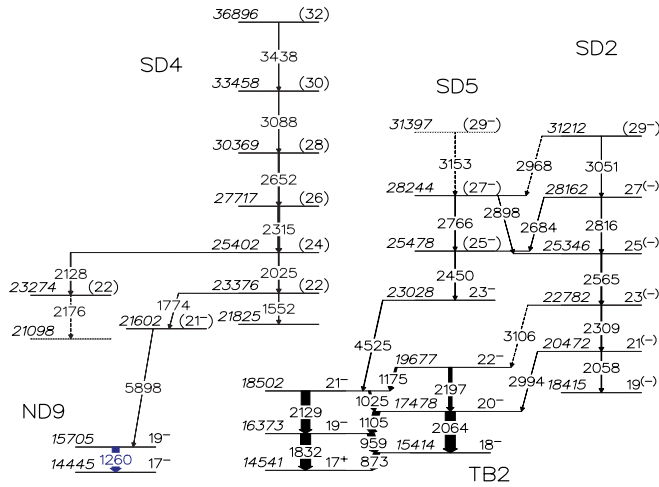
FIG. 17. (Color online) Decay scheme of the superdeformed bands SD4 and SD5 of the level scheme of ^{62}Zn. Energy labels are in keV and tentative levels and transitions are dashed. The widths of the arrows correspond to the relative intensities of the γ rays.

K. The superdeformed bands SD4 and SD5

One more superdeformed structure labeled SD4 has been observed in data set 1. Furthermore, a sequence of levels interacting with the central section of SD2 could be observed, which is denoted SD5. The respective part of the high-spin level scheme of ^{62}Zn is shown in Fig. 17.

SD4 comprises a sequence of six transitions ranging from 1552 to 3438 keV. The DCO ratios of the four central transitions of SD4 are consistent with $E2$ character. The two lowest transitions are paralleled with a 2176- to 2128-keV sequence. The level at 23 378 keV decays via a 1774- to 5898-keV cascade into the yrast 19$^-$ state at 15 705 keV in ND9. Based on yrast arguments, the nearly 6-MeV link is suggested to have quadrupole character. The DCO ratio measured for the transition at 1774 keV is indicative of dipole character. Thus, SD4 is associated with even-spin values, in the range of $I = 20\hbar$–$32\hbar$. Its levels reach excitation energies up to 37 MeV. Note that it has not been possible to add any transition on top of SD4 by investigating data set 2.

Figure 18 provides γ-ray spectra considered relevant for the decay pattern of SD4. The spectrum in Fig. 18(a) is in coincidence with the 5898-keV linking transition. Besides intense peaks at, for example, 1197, 1232, 1340, or 1522 keV, Fig. 18(a) shows a distinct peak at 1260 keV, which marks the feeding into the already-mentioned yrast 19$^-$ state at 15 705 keV in ND9. Consistent with that observation is the presence of admittedly weak lines at 1633, 2437, and 2483 keV. Additionally, the lowest transitions in SD4 at 1774, 2025, 2315, and 2652 keV are observed with anticipated decreasing yield. The inset of Fig. 18(a) highlights the placement of the 5898-keV linking transition: It is a spectrum in coincidence with either the 1260-keV (ND9) or 1774-keV (SD4) lines, both contributing comparable statistics to the distinct peak at 5898 keV.

The 1552-keV transition at the bottom of SD4, the 2128- to 2176-keV side branch, and the 3088- and topmost 3438-keV transitions are evidenced in Fig. 18(b): The main spectrum
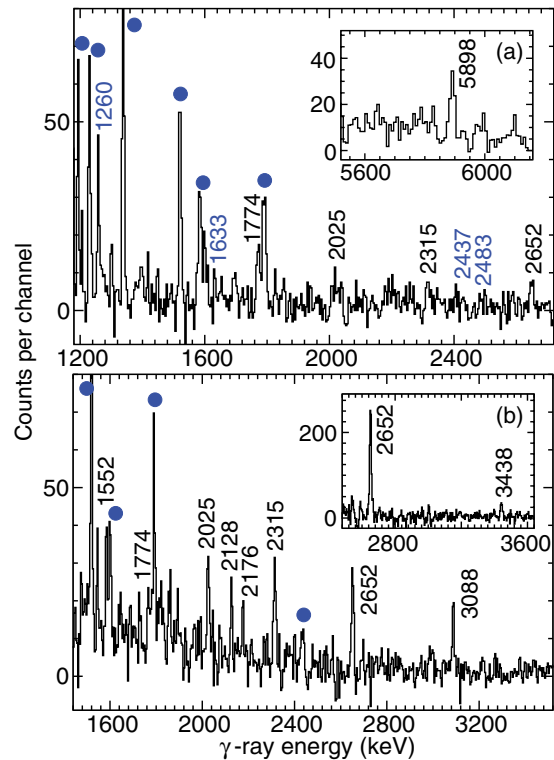

FIG. 18. (Color online) (a) γ-ray spectrum in coincidence with the 5898-keV decay-out transition of SD4. The inset shows the high-energy part of a spectrum in coincidence with either 1260 or 1774 keV. (b) γ-ray spectrum in coincidence with any combination of two out of the four main members of the band SD4 at 2025, 2315, 2652, and 3088 keV. The inset shows a portion of the spectrum in coincidence with the 3088-keV transition. Energy labels are in keV. Blue labels and solid circles mark transitions belonging to the ND part of the ^{62}Zn level scheme. The binning is 4 keV per channel except for the inset of panel (a), where it is 8 keV per channel.

is in coincidence with various combinations of transitions in SD4. The spectrum in the inset is only in coincidence with the 3088-keV transition. Here, both the feeding and depopulating transitions at 3438 and 2652 keV, respectively, can be seen.

Finally, Fig. 19 focuses on the newly observed band SD5, which is intimately related to the known band SD2. Building on the 4525-keV $E2$ transition, which feeds the 21$^-$ state at 18 502 keV in TB2, transitions at 2450 2684, 2766, 2968, and 3051 keV are observed in coincidence, as shown in Fig. 19(a). The position of the 4525-keV link in the level scheme can be evidenced by Fig. 19(b), which is a spectrum taken in coincidence with both the transitions placed below (2129-keV line in TB2) and above (2450-keV line in SD5).

Lines at 2450, 2766, and (tentatively) 3153 keV form the sequence SD5, while the 2684- and 2968-keV transitions connect SD2 with SD5. This becomes clear not only by the 3051-keV transition belonging to SD2, but also the corresponding 2898-keV transition, which forms the connection from SD5 to SD2 in the crossing regime at spin $I \sim 25\hbar$–$27\hbar$ (cf. Fig. 3(a) of Ref. [18]). Not only is it a function of the interband transitions to establish the placement of SD5 in the complex decay scheme, but they also guide the (tentative) spin
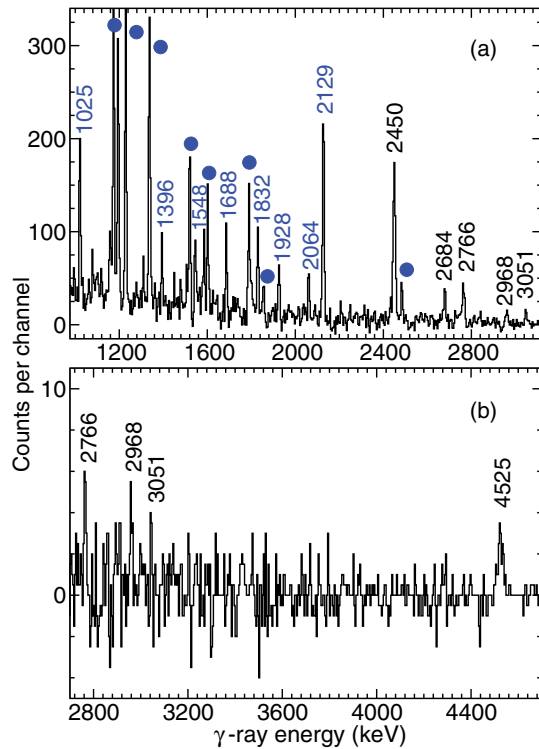
FIG. 19. (Color online) (a) γ-ray spectrum in coincidence with the 4525-keV decay-out transition of SD5. (b) γ-ray spectrum in coincidence with the 2129-keV transitions in TB2 and the 2450-keV transition in SD5. Energy labels are in keV. Blue labels mark transitions associated with TB2 and blue solid circles mark transitions belonging to the ND part of the ^{62}Zn level scheme. The binning is 4 keV per channel.

and parity assignments, especially in combination with the DCO ratio of the 4525-keV linking transition, which clearly favors $E2$ character.

IV. INTERPRETATION OF THE OBSERVED BANDS

The observed bands were analyzed using the configuration-dependent cranked Nilsson-Strutinsky (CNS) formalism [42–44]. This approach is based on a modified oscillator potential which is cranked around the x axis. Deformations are included by allowing the three oscillator frequencies to be different corresponding to ellipsoidal shapes described by the quadrupole parameters, ε_2 and γ [45]. Furthermore, one hexadecapole deformation degree of freedom is included. It is described by ε_4 and parametrized in such a way that axial symmetry at prolate and oblate shape is not broken [46]. Standard parameters [42] are used for the single-particle parameters, κ and μ.

Single-particle energies are calculated in a mesh in deformation and rotational frequency, $(\varepsilon_2, \gamma, \varepsilon_4, \omega)$. The Strutinsky method is applied [47,48]; that is, the total energies are obtained as the sum of the shell energy and the rotating liquid drop energy. The static liquid-drop parameters are taken from the Lublin-Strasbourg drop (LSD) [44,49]. The rigid moments of inertia are calculated from a nucleus with diffuse surface [44,50].

Because of the simplicity of the modified oscillator potential, it is possible to fix configurations in a detailed way, using exact as well as approximate quantum numbers. An important feature is that the exact solutions of the rotating harmonic oscillator are used as basis states in the single-particle diagonalization. It turns out that the couplings between states which differ by the principal quantum number $\mathcal{N}_{\text{rot}}$ in this basis are small in the rotating modified oscillator potential. They can therefore be neglected; that is, $\mathcal{N}_{\text{rot}}$ is treated as a preserved quantum number in the CNS formalism. Because $\mathcal{N}_{\text{rot}}$ becomes equal to $\mathcal{N}_{\text{osc}} \equiv \mathcal{N}$ defined for the static oscillator at $\omega = 0$, we refer to this quantum number as $\mathcal{N}$ below. The signature (exponent) quantum number α is preserved taking the values $\alpha = 1/2$ and $\alpha = -1/2$ [43,51], with the total signature of a system defined from the sum of the signatures for the occupied orbitals,

$$\alpha_{\text{tot}} = \alpha = \left(\sum_{\text{occ}} \alpha_i \right) \text{mod} 2.$$

Finally, within each $\mathcal{N}$-shell, it is generally possible to distinguish between orbitals which have their main amplitudes in the high-j intruder shell and the low-j orbitals which have their main amplitudes in the other j shells, thus defining an additional approximate quantum number.

The j shells which determine the structure of ^{62}Zn are the $\mathcal{N} = 3$ high-j $1f_{7/2}$ shell, the low-j fp shells $1f_{5/2}$, $2p_{3/2}$, and $2p_{1/2}$, and finally the $\mathcal{N} = 4$ shell $1g_{9/2}$. The $2p_{1/2}$ shell can essentially be neglected owing to its low-j value and its high energy in the Nilsson diagram. The j shells are pure only if the shape is spherical. In the deformed rotating potential, the j shells will mix; that is, in the present approximation the wave functions of the single-particle orbitals will have amplitudes in all the j shells of a specific $\mathcal{N}$-shell. However, as stated above, it turns out that if the deformation is not too large, these orbitals can be classified as having their main amplitudes in either the high-j intruder shell or in the other shells with smaller j values [43,52]. Therefore, configurations can be specified relative to a ^{56}Ni core as

$$\pi[(1f_{7/2})^{-p_1}(fp)^{p_3}(1g_{9/2})^{p_2}]$$
$$\otimes \nu[(1f_{7/2})^{-n_1}\nu(fp)^{n_3}(1g_{9/2})^{n_2}], \qquad (3)$$

that is, by the number of particles and holes in the j shells above and below the $Z = N = 28$ gap.

One may note that to define a configuration, also the distribution over the two signatures within the respective groups must be specified. However, an even number of particles within a group is generally distributed equally over the two signatures for the low-energy configurations. Furthermore, with only a few particles in an even (odd) $\mathcal{N}$-shell, the orbitals with $\alpha = 1/2$ ($\alpha = -1/2$) are strongly favored in energy. Therefore, one or three protons or neutrons in $1g_{9/2}$ will contribute with $\alpha = 1/2$ in the low-energy configurations. With a few holes in a high-j orbital, however, the two signatures are essentially degenerate; that is, two signature degenerate bands will be formed with one (or three) hole in $f_{7/2}$. With this in mind, we, in general, specify configurations as

$$[p_1 p_2(\pm), n_1 n_2(\pm)],$$

with the numbers p_1, p_2, n_1, n_2 defined in Eq. (3) and with the signature of an odd number of fp protons or neutrons specified in parentheses as $+$ or $-$ for $\alpha = 1/2$ and $\alpha = -1/2$, respectively. Note that the numbers p_3 and n_3 are determined according to $p_3 = 2 + p_1 - p_2$ and $n_3 = 4 + n_1 - n_2$ for ^{62}Zn. Furthermore, the general feature of a configuration is determined by $q_1 = p_1 + n_1$ and $q_2 = p_2 + n_2$ [10]. For a configuration defined by Eq. (3), it is useful to define I_{max}, which is the highest possible spin in the pure j-shell configuration.

In the CNS approach, the total energy for each configuration is minimized in terms of deformation using the parameters specified above. The calculations do not include pairing. Therefore, they are realistic only at high spins, but they also give a qualitative understanding of the low-spin states. Comparing with the shell model where residual interactions between configurations are included, only long-range multipole interactions are included in the present mean-field approach. Another approximation is that the angular momentum is identified with the expectation value along the rotation axis. With these approximations, the number of particle-hole excitations is practically unlimited in the CNS formalism.

A. General features of observed bands

The observed bands in ^{62}Zn are drawn relative to the rotating liquid drop energy in Fig. 20 for positive (a) and negative (b) parity, respectively. As noted above, the WD6 and WD7 bands interact around $I^\pi = 21$, where their energy difference is only 20 keV. To make these band energies smooth, WD6 and WD7 bands should cross at the 21^- spin state. In this process, two smooth undisturbed bands with new energies called WD6-7 and WD7-6 are formed, which are drawn in Fig. 20(b). These "undisturbed" bands are compared with the calculated CNS bands below. The energy of the two undisturbed bands at $I = 21$ should fall in between the observed energies for WD6 and WD7. It is not really possible to determine which values are most appropriate and the exact value chosen does not make any visible difference in the scale of Fig. 20(b), where both bands are given the average of the energies of bands WD6 and WD7 at $I = 21$.

As it is only the $\mathcal{N} = 3$ and $\mathcal{N} = 4$ shells that are open (with a possible exception of the very highest spin states), the positive-parity bands have an even number of particles and the negative-parity bands have an odd number of particles in these $\mathcal{N}$-shells. Within each group of bands with the same number of $\mathcal{N} = 4$ particles, a division can be made into groups of bands with the same number of $1f_{7/2}$ holes. For the general assignment, one notes the following [43].

(i) The maximum spin in the bands increases with both q_1 and q_2.

(ii) The addition of the first particles in a high-j shell ($1g_{9/2}$ in the $A = 60$ region) will correspond to a lower energy cost for the highest spin states in the bands; that is, the band will be more downsloping for spin values close to I_{max} when drawn relative to the rotating liquid drop energy.

(iii) The addition of the first holes in a high-j shell ($1f_{7/2}$ in the $A = 60$ region) will have the opposite effect, that
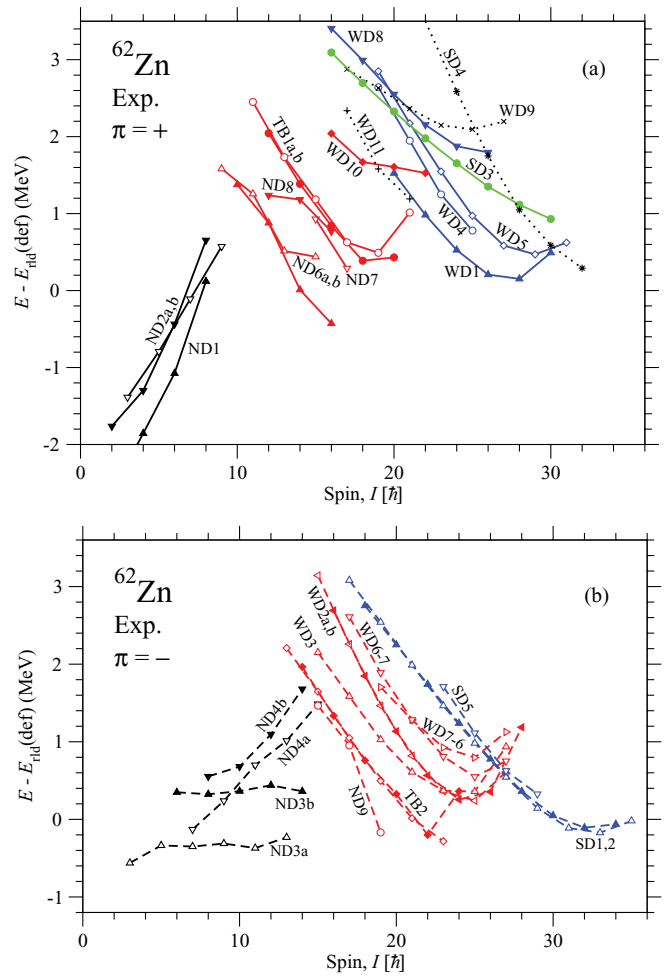

FIG. 20. (Color online) Observed states in ^{62}Zn shown relative to a rotating liquid drop reference. States with positive parity are drawn by full lines in panel (a) while those with negative parity are drawn with broken lines in panel (b). Bands with undefined parity are drawn in panel (a) with dotted lines. Solid symbols are used for even-spin states ($\alpha = 0$) and open symbols for odd-spin states ($\alpha = 1$). Symbols and colors are used to indicate the number of $1f_{7/2}$ and $1g_{9/2}$ particles in the configurations assigned to the bands.

is, a higher-energy cost for spin values close to I_{max} corresponding to a larger upslope of $E - E_{rld}$ close to I_{max}. In general, this will lead to a stronger curvature of $E - E_{rld}$ equivalent to a smaller value the $\mathcal{J}^{(2)}$ moment of inertia.

Except for the SD bands, the rotational bands are generally observed (close) to termination, that is, to spin values up to I_{max} or possibly $I_{max} - 2$. Following the rules above, it is straightforward to classify the bands into $[q_1/q_2]$ groups as demonstrated in Fig. 20, where they are drawn by different colors depending on the value of q_2. This division is made from the observation that the bands with 0, 2, and 4 $1g_{9/2}$ particles have maximum spin values up to $I_{max} \approx 10, 22$ and $I_{max} > 30\hbar$, respectively, while the bands with 1, 3, and 5 $1g_{9/2}$ particles have maximum spin values up to $I_{max} \approx 16, 28$ and $I_{max} > 33\hbar$, respectively. Within a group of bands with the same number of $1g_{9/2}$ particles, the bands with the same

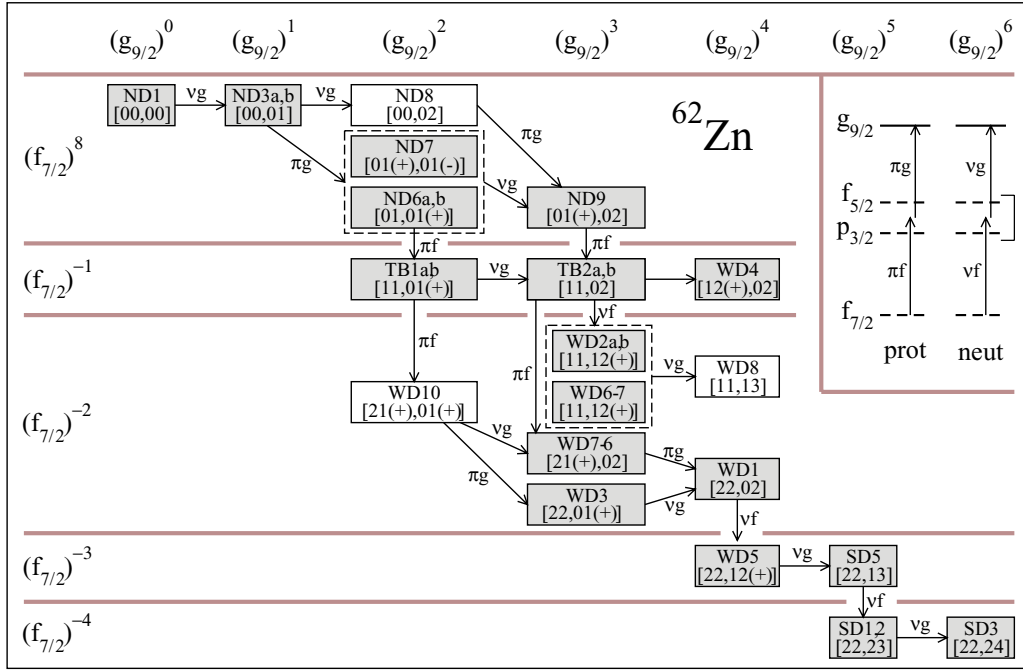FIG. 21. (Color online) Suggested configurations for the observed bands in ^{62}Zn grouped according to the number of holes in the $1f_{7/2}$ orbitals and particles in the $1g_{9/2}$ orbitals. More detailed configurations are given in each case specifying the distribution over protons and neutrons where boxes with configurations that appear well established are shaded. Starting from the [00, 00] ground-state configuration, arrows indicate how the observed bands are created from successive proton and neutron excitations (see inset) from the fp orbitals to the $1g_{9/2}$ orbitals (πg and νg) and from the $1f_{7/2}$ orbitals to the fp orbitals (πf and νf).

number of $1f_{7/2}$ holes are drawn by similar symbols; circles, triangles, and diamonds, respectively. This classification is also straightforward considering the highest observed spin values and the curvature and slope close to termination.

With this general characterization of the bands, the detailed calculations are carried out mainly to determine how the holes and particles are distributed over protons and neutrons and also with which accuracy it is possible to describe the energies for the different spin values. The classification of the bands suggested in Fig. 20 is specified in more detail in Fig. 21. There the bands are arranged in groups according to the values of q_1 and q_2 but specifying configurations in terms of holes and particles for protons and neutrons according to the interpretation below. Of special interest is the fact that starting from the configuration with all valence particles in the fp orbitals ($q_1 = q_2 = 0$), one can continuously follow how bands are formed from excitations of protons or neutrons from the $1f_{7/2}$ orbitals to the fp orbitals or from the fp orbitals to the $1g_{9/2}$ orbitals. The nucleus ^{62}Zn appears very special in this context, with a continuous evolution from low-spin bands of small collectivity over more strongly deformed bands and up to superdeformed bands.

B. The structures with $I_{\max} \leqslant 25\hbar$

The experimental energies with the rotating liquid drop energy subtracted are shown as a function of spin for the observed positive-parity bands ND1, ND6, ND7, ND8, TB1, and WD4 with $I_{\max} \leqslant 25\hbar$ in the top panel of Fig. 22. Similarly,

the observed negative-parity bands ND3, ND9, and TB2 with $I_{\max} \leqslant 25\hbar$ are shown in the top panel of Fig. 23. In both Figs. 22 and 23, the middle panel shows the selected calculated bands with the energy difference between calculations and experiment in the bottom panels. These bands are formed by successive excitations of particles to the $1g_{9/2}$ subshell and from the excitation of at most one proton from the $1f_{7/2}$ orbitals. The interpretation of the ND1, ND3, ND6, ND9, TB1, and TB2 bands was given already in Ref. [20]. There the 13^+ state of ND6a was placed at a higher energy than in the present level scheme, but one notes that the present energy fits much better with calculations, suggesting that the ND6a and ND6b bands are essentially signature degenerate. However, also a 15^+ state has now been observed, which breaks the trend of signature degeneracy. Indeed, the calculations predict a favored termination of the ND6a structure in a 15^+ state and it appears somewhat strange that no such state is observed.

The new structure ND7 with a 15^+ and a 17^+ state is quite interesting. The 17^+ state is fed by a lot of weak transitions, which strongly suggests that it is a terminating, fully aligned state (see Ref. [53]). In fact, 17^+ is the highest spin state which can be formed in a configuration with no $1f_{7/2}$ holes and two $1g_{9/2}$ particles, namely in the configuration

$$\pi\big[(fp)^1_{5/2}(1g_{9/2})^1_{9/2}\big] \otimes \nu\big[(fp)^3_{11/2}(1g_{9/2})^1_{9/2}\big], \qquad (4)$$

where the spin contribution from the different groups of particles is given as subscripts. However, as seen in Fig. 22, this 17^+ state is calculated at a much too high energy compared with experiment. This high energy is understood
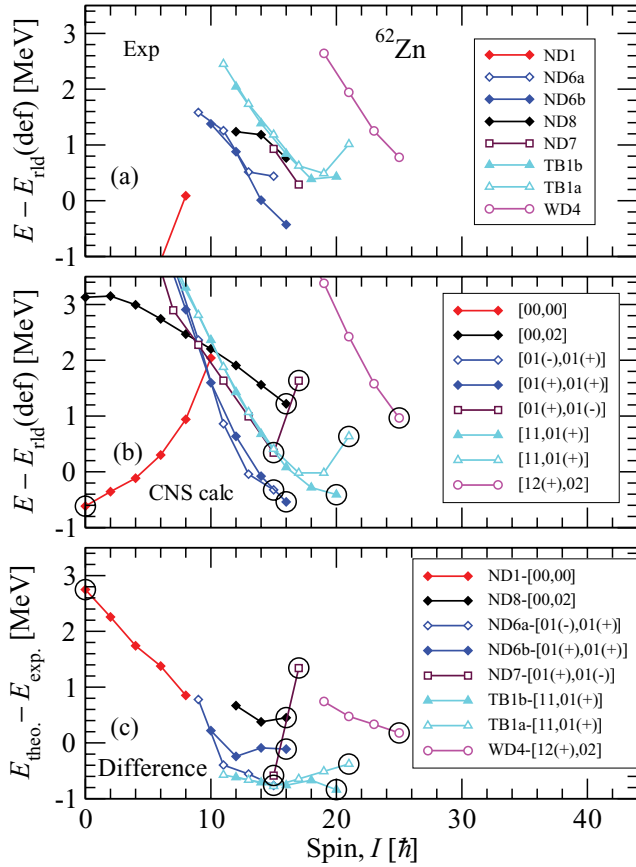
FIG. 22. (Color online) The top panel displays the energy of the experimental rotational bands, ND1, ND6, ND7, ND8, TB1, and WD4 with positive parity as a function of spin, while the middle panel shows the theoretical bands assigned to them. The bottom panel shows the difference between the experimental and theoretical bands. Solid symbols are used for even-spin states and open symbols for odd spin states.

from Fig. 24, which is drawn at a deformation typical for the fully aligned states of the [01,01] configurations. The straight line representing the Fermi surface in the figure defines a favored neutron state with $I_n = 9^-$, that is, with signature $\alpha_n = 1$. When combined with the aligned $I_p = 6, 7$ proton states, it gives rise to the calculated low-lying aligned $I = 15, 16$ states of the [01($\pm$), 01(+)] configuration which are assigned to the ND6 bands. However, when forming an aligned neutron configuration of signature $\alpha_n = 0$ instead, the $m_i = 1/2$ neutron can be moved either to the $m_i = -1/2$ state or to the $m_i = 3/2$ state as illustrated by arrows in Fig. 24. It is apparent that the $I_n = 8$ state is about as favored as the $I_n = 9$ state while the $I_n = 10$ is much less favored in energy because the $m_i = 3/2$ single-particle state is considerably higher in energy relative to the straight-line Fermi surface. Consequently, when combined with the proton $I_p = 7$ state, the resulting $I = 15$ state is relatively low in energy while the $I = 17$ state is relatively high in energy. The high energy of this $I = 17$ state [see Eq. (4)] is in disagreement with the low energy of the terminating $I = 17$ state of the ND7 structure, giving strong arguments that the energy of the $1f_{5/2}$ shell must be lowered relative to the $1p_{3/2}$ shell (see Fig. 24).
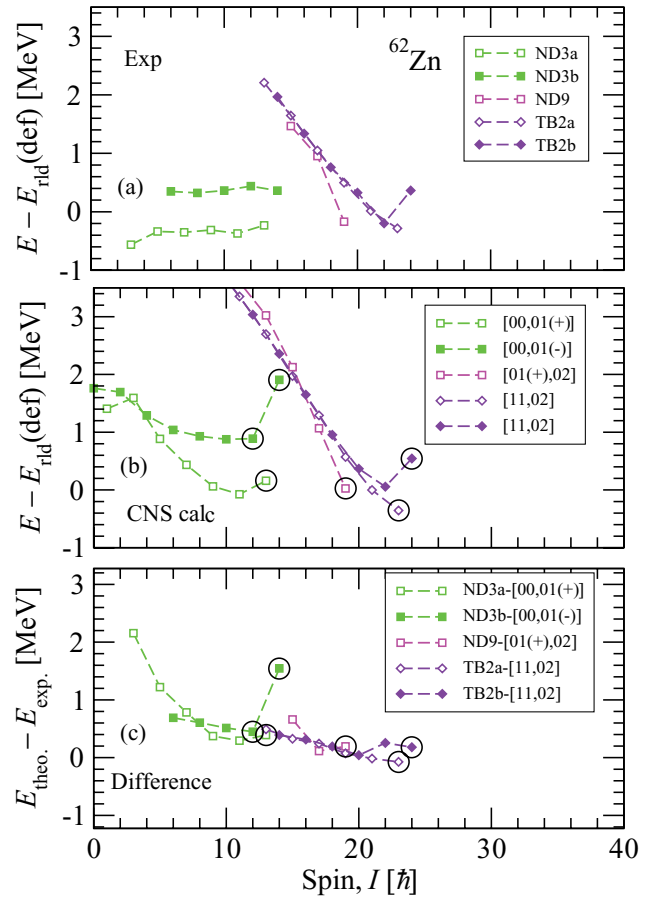

FIG. 23. (Color online) Same as Fig. 22, but here for the observed bands with negative parities ND3, ND9, and TB2.

The 12^- and 14^- states of structure ND3b are also new compared with Ref. [20]. One notes that $I = 14^-$ is the highest possible spin in the [00, 01] configurations in a similar way as $I = 17^+$ is the highest spin in [01, 01] configurations. These two fully aligned states have the same neutron configuration with $I_n = 10$ (see Fig. 24). Consequently, the low energy of the 14^- state of structure ND3 is another indication that the $1f_{5/2}$ and $1p_{3/2}$ shells should come closer together.

The ND8 structure is built from only three states, $I = 12^+$, 14^+, and 16^+. It is furthermore irregular and therefore difficult to assign to any specific configuration even though one can conclude that it must have two $1g_{9/2}$ particles and no holes in the $1f_{7/2}$ orbitals. It is compared with the [00, 02] configuration in Fig. 22, which has $I_{max} = 16$. Another possibility is to assign it to the fourth [01, 01] band, namely [01(−), 01(−)].

The two previously observed [20] terminating structures, TB1 and TB2, are built from close-to-signature degenerate bands connected by $M1$ transitions. They are well described [20] by the configurations [11,01(+)] and [11,02], respectively, but their relative energies indicate that with present parameters, the energy cost is too high to excite a neutron to the $1g_{9/2}$ shell.

Band WD4 is strongly downsloping when drawn relative to the rotating liquid drop energy. It is observed to $I = 25^+$,
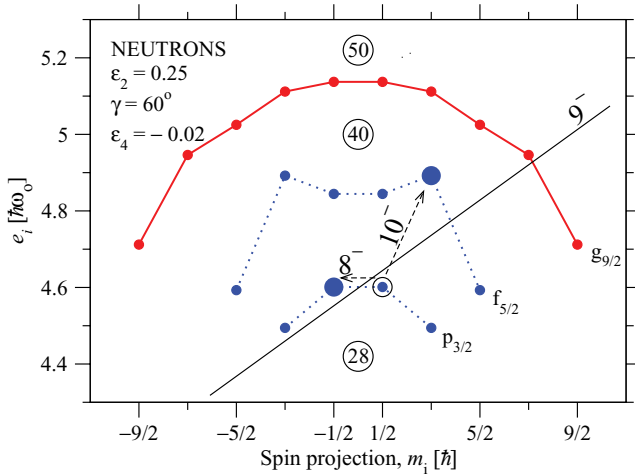
FIG. 24. (Color online) Sloping Fermi surface diagram at a deformation typical for the terminating [01, 01] states of ^{62}Zn. Favored aligned states are formed in configurations defined by straight-line, or close-to-straight line Fermi surfaces, where all orbitals below the Fermi surface are occupied and those above are empty, so-called optimal states [48]. Such an optimal state is formed at $I_n = 9$ in the $\nu(fp)^3(g_{9/2})^1$ configuration, as illustrated in the figure. Particle-hole excitations to $I_n = 8$ and $I_n = 10$ are indicated by arrows, where the distance to the Fermi surface shows that the former state is more favored in energy than the latter.

which is the highest possible odd spin state in the [12,02] configurations. The observed energies are well described by this [12(+),02] band, with signature $\alpha = +1/2$ for the $1f_{7/2}$ proton hole, which is calculated to be clearly favored in energy at high spin values compared with the other [12,02] bands. Therefore, the WD4 band is assigned to this [12(+),02] configuration. One could note, however, that in the spin range $I = 19$–25, where both bands WD4 and WD5 are observed, these two bands are very similar in energy (see Fig. 20). Then, however, WD5 is observed to higher spin values which shows that it must be assigned to a configuration with more $1f_{7/2}$ holes. Therefore, it cannot be excluded that WD4 should also be assigned to a similar configuration with more $1f_{7/2}$ holes (see below).

The bands ND2 and ND4 appear to be rather vibrational than rotational, so we do not try to assign any CNS configurations to them.

As mentioned earlier, neglecting the pairing force results in less reliable energy predictions for low-spin structures. This can be observed in both Figs. 22 and 23. As spin increases, the bands in the lowest panel tend to move towards a smaller absolute energy difference. Indeed, above $I = 8$, the differences in the bottom panels of Figs. 22 and 23 are fairly constant for the different structures and fall within ± 1 MeV except for the highest spin states in the ND3 and ND7 configurations. As discussed above (see also Ref. [41]) these highest-spin states are formed with the third fp neutron in the $1f_{5/2,m=3/2}$ orbital and it appears unlikely that the large energy difference for these states are caused by the neglect of pairing correlations. Thus, it seems that pairing correlations are essentially negligible for spin values $I > 8$ in ^{62}Zn.

C. Well-deformed structures with $I_{max} \leqslant 30\bar{h}$

In the earlier studies [17,20] of the high-spin structure of ^{62}Zn, no states were observed between the terminating bands with one $1f_{7/2}$ hole and the SD bands which typically have four such holes. A large number of such bands referred to as well-deformed have now been discriminated experimentally. The bands with two $1f_{7/2}$ holes can have either one proton hole and one neutron hole or both holes in the proton orbitals. The calculated low-lying bands of this type are shown in the top and bottom panels of Fig. 25, respectively. In these configurations, one can see a clear division into orbitals with two, three, and four $1g_{9/2}$ orbitals, having their energy minima at $I \approx 18$, $I \approx 23$, and $I \approx 27$, respectively. Note also that with one proton hole and one neutron hole, four bands which are essentially signature degenerate are formed because of the two signatures for both holes. Comparing with experiment, it turns out that one can find correspondences to most of the bands which are calculated low in energy. This is illustrated in Figs. 26 and 27.
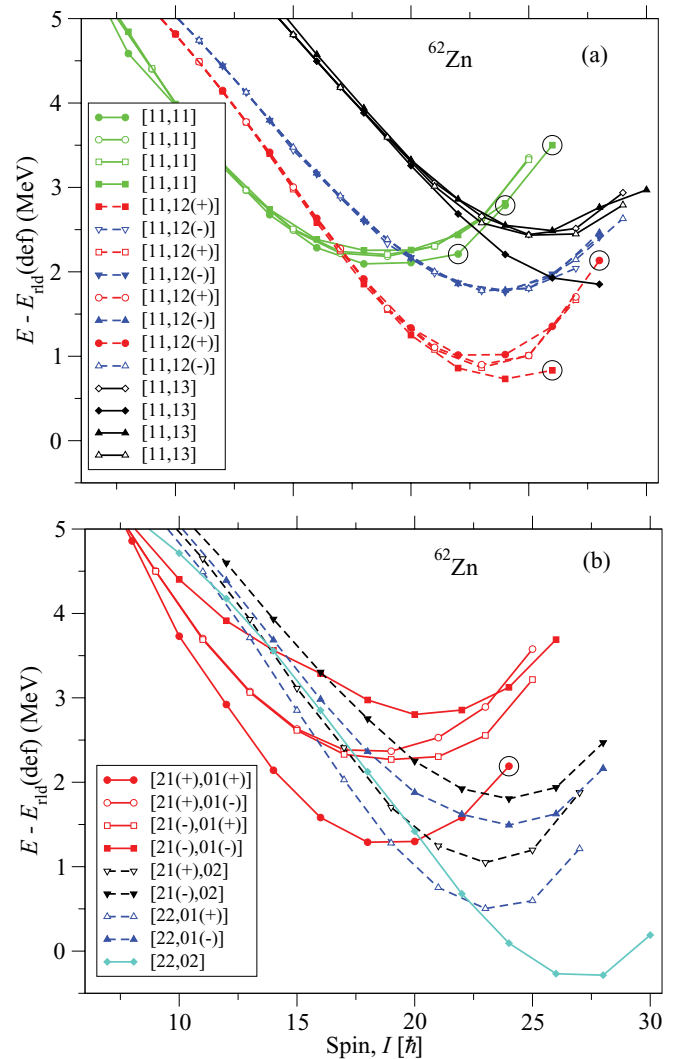

FIG. 25. (Color online) Low-lying calculated bands with two holes in $1f_{7/2}$; one proton and one neutron hole in panel (a) and two proton holes in panel (b). The convention for full and broken lines and closed and open symbols is the same as in Figs. 20, 22, and 23.
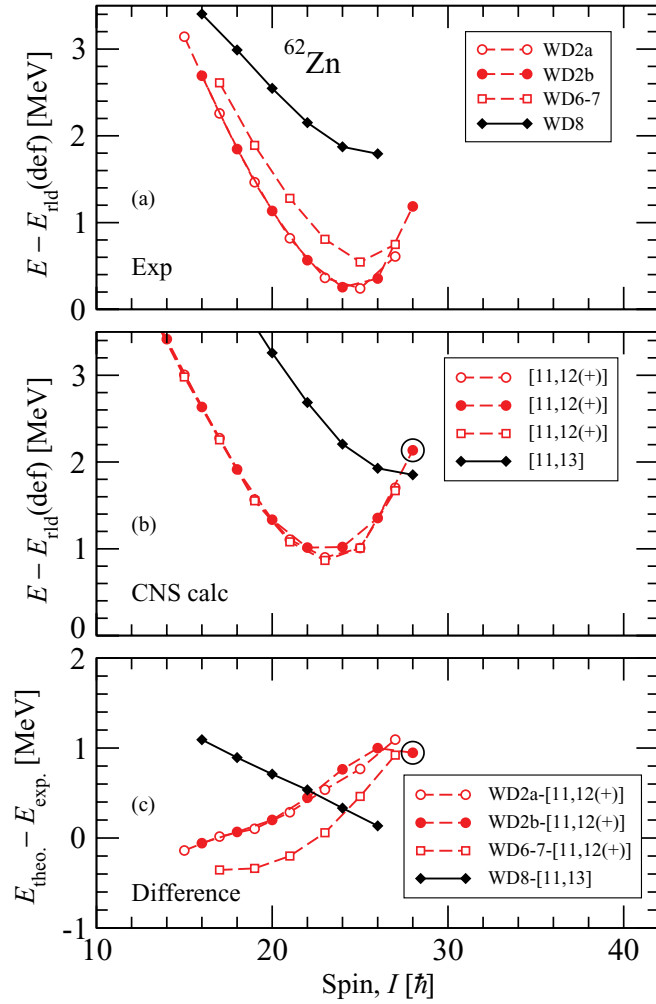
FIG. 26. (Color online) Same as Fig. 22 but for positive- and negative-parity high-spin deformed structures assigned to configurations with one proton and one neutron hole in $1f_{7/2}$ orbitals.
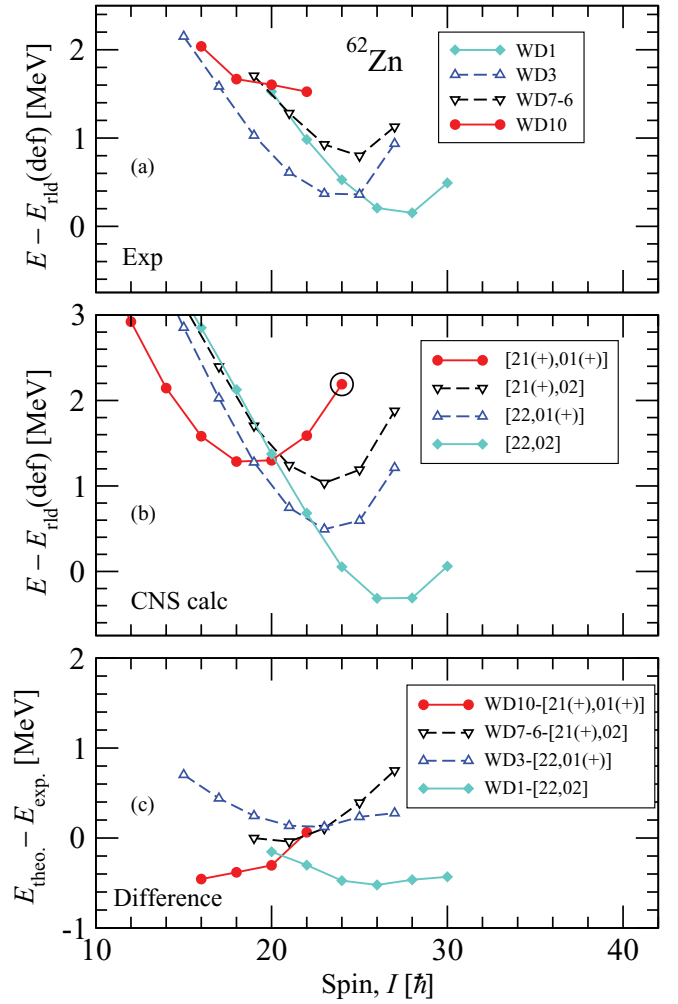

FIG. 27. (Color online) Same as Fig. 22 but for positive- and negative-parity high-spin deformed structures assigned to configurations with two proton holes and no neutron hole in $1f_{7/2}$ orbitals.

The signature degenerate bands WD2a and WD2b are naturally assigned to two of the $[11,12(+)]$ bands with $I_{max} = 27^-$ and 28^-. Furthermore, it appears that the WD6-7 structure can be assigned to the other $[11,12(+)]$ band with signature $\alpha = 1$. Note that the four calculated $[11,12(+)]$ bands are degenerate in a large spin range, but that one would expect an interaction between the bands of the same signature which is not included in the CNS approach. This interaction would lead to an energy difference in general agreement with the difference observed between bands WD2a and WD6-7. Then, however, the assignment would be even more convincing if a signature degenerate partner to band WD6-7 was also observed. Furthermore, the upslope in the energy differences in the bottom panel of Fig. 26 points to a discrepancy between calculations and experiment which is unexpectedly large considering the general success of the CNS approach in different mass regions [43,44].

The low-energy configurations with two $1f_{7/2}$ proton holes are illustrated in the bottom panel of Fig. 25. They show some kind of mirror symmetry between the proton and neutron configurations because they will have four protons and four

neutrons in the fp and $1g_{9/2}$ orbitals. It is then instructive to consider the single-particle orbitals in Fig. 28. The conclusion from that figure is that the low-energy configurations of this type will have two fp particles and one $1g_{9/2}$ particle; that is, they can be described as a core with 29 protons and 31 neutrons,

$$\pi(f_{7/2})^{-2}(fp)^2(g_{9/2})^1\nu(fp)^2(g_{9/2})^1,$$

with one "odd" proton and one "odd" neutron outside.

The $Z = 29$ proton configuration is formed at the large gap at the frequency $\hbar\omega \sim 1.2$ MeV, while the $N = 31$ neutron configuration has the same orbitals filled as the proton configuration and in addition two particles in the $(f_{7/2})_4$ orbital (see Fig. 28). Low-energy bands are now obtained if the odd proton and neutron is placed either in the $\alpha = +1/2$ $(fp)_2$ orbital or in the $\alpha = 1/2(g_{9/2})_1$ orbital, which thus leads to four combinations. These four bands can all be assigned to observed bands (see Figs. 25 and 27); WD1 with both particles in the $1g_{9/2}$ orbitals, WD3 and WD7-6 with only one $1g_{9/2}$ particle, and WD10 with both particles in the fp orbitals. The agreement is convincing although the differences
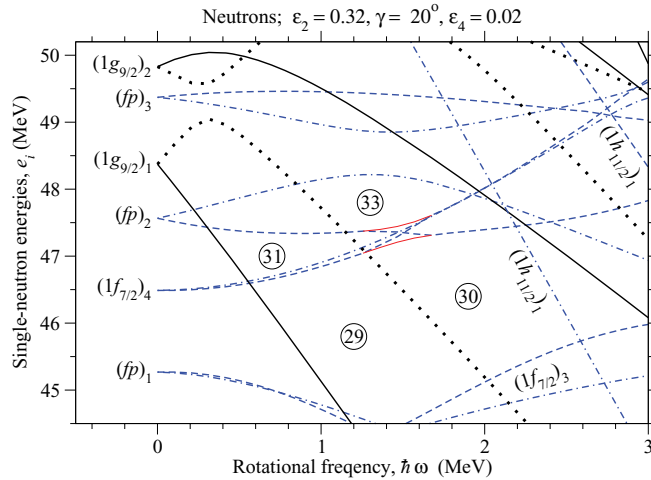
FIG. 28. (Color online) Calculated neutron single-particle routhians plotted as a function of rotational frequency at the deformation $\varepsilon_2 = 0.32$, $\gamma = 20°$, $\varepsilon_4 = 0.02$. Particle numbers at some gaps are encircled. The orbitals are labeled by the group to which they belong and the ordering in the group at rotational frequency, $\omega = 0$. So called virtual crossings have been removed but the noncrossing $(f_{7/2})_4$ and $(fp)_2$ orbitals at $\hbar\omega \approx 1.5$ MeV are shown by full lines. Dashed lines are used for negative parity and dots indicate signature $\alpha = -1/2$.

in the bottom panel of Fig. 27 are rather scattered but within the expected accuracy of ± 1 MeV. Furthermore, the highest spin $I = 22^+$ state of the WD10 band does not follow the expected trend of the lower spin $I = 16, 18, 20$ states. Indeed, an alternative assignment for WD10 would be an [11,11] band with even spin values. As seen in Fig. 25, these [11,11] bands are calculated only a few hundred keV higher in energy than the [21(+),01(+)] band, which is compared with WD10 in Fig. 27.

Band WD8 is observed to $I = 26$ and has positive parity, which means that it must have 4 $1g_{9/2}$ particles. One possibility is that it should be assigned to the highest spin band of the [12,02] configuration with $I_{\max} = 26$ in a similar way as the WD4 band is compared to the signature partner with $I_{\max} = 25$ in Fig. 22. Instead, it appears more plausible that it has two $1f_{7/2}$ holes. It is thus compared with the lowest [11,13] configuration with $I_{\max} = 28$ in Fig. 26. There are, however, other similar bands calculated a few hundred keV higher in energy. These are either of the type [12,12] or of the type [22,02] with a broken pair compared with the low-energy configuration assigned to the WD1 band. Thus, the configuration of the WD8 band remains uncertain.

D. Superdeformed structures

1. Difficulties with configuration assignments

The classification of orbitals as high-j or low-j [43,52] is rather straightforward at small deformations, say $\varepsilon_2 < 0.3$, while it is not possible at very large deformations. The regularity of the superdeformed bands in ^{62}Zn indicates that this classification is relevant; however, it is rather difficult to carry through in the numerical calculations. The difficulties are illustrated Fig. 28 where the neutron orbitals are drawn at

the deformation $\varepsilon_2 = 0.32$, $\gamma = 20°$, $\varepsilon_4 = 0.02$. It is obvious that there is a rather large interaction between the $\alpha = 1/2$, $(1f_{7/2})_4$ and $(fp)_2$ orbitals at the frequency $\hbar\omega \approx 1.5$ MeV. Therefore, using our standard programs, it is questionable if a real crossing will be created between these orbitals. For smaller deformations a crossing will be created, which makes it straightforward to make a correct classification of $1f_{7/2}$ and fp orbitals at all frequencies. At larger deformations, however, no crossing is created and the division into low-j and high-j orbitals will be different (and erroneous) because it is fixed at low frequencies, which means that it will be different at high frequencies depending on if these orbitals cross or not. In the numerical calculations where the energy is interpolated over a region in the (ε_2, γ) plane, large discontinuities will occur if the crossings are not treated in the same way in the full region and the result will be more or less meaningless.

One possibility is then not to create any crossings between low- and high-j orbitals. In this case, where the configurations are only characterized by the number of $\alpha = 1/2$ and $\alpha = -1/2$ particles in the different $\mathcal{N}$-shells, the potential energy surfaces might have two minima which are characterized by a different division over high-j and low-j orbitals. There is, however, also the possibility that these "bands" will have very similar deformations, in which case only one minimum will be seen in the energy surfaces and the higher energy band can instead be identified as an excited state in the configuration. This was the procedure followed in Ref. [18], where the SD bands in ^{62}Zn were identified from a careful investigation of the potential energy surfaces of the lowest as well as second-lowest states for configurations defined with no distinction between high-j and low-j orbitals.

The procedure used in Ref. [18] is time consuming and not applicable in all cases. Therefore, in the present calculations, we have instead made changes in our crossing programs, forcing the $(1f_{7/2})_4$ and $(fp)_2$ orbitals to cross even if they never come very close in the crossing region. In the forced crossing in Fig. 28, the $(fp)_2$ orbital is somewhat irregular and such irregularities will be more accentuated and lead to numerical errors at larger deformations. However, it appears that the calculated configurations will avoid such regions (of high level density) where an irregular crossing is formed. Thus, with this method to force a crossing, the bands come out almost the same as in Ref. [18], but using a method which is faster and more general and which can easily be applied, for example, to the neighbor nuclei of ^{62}Zn.

2. Classification of the observed superdeformed structures

In the single-particle diagram provided in Fig. 28 there is a large gap at large deformation for particle number 30. This gap corresponds to the $(1f_{7/2})^{-2}(fp)^2(1g_{9/2})^2$ configuration, leading to the "doubly magic" superdeformed band in ^{60}Zn [15]. Above this gap, there are two (fp) orbitals, two $1f_{7/2}$ orbitals, and one $\alpha = 1/2$ $1g_{9/2}$ orbital at similar energies. One may note that the superdeformed band observed in ^{65}Zn is assigned to the configuration where the five neutron orbitals listed above are occupied in addition to the proton and neutron orbitals below the gap at $Z = N = 30$ [54]. In ^{62}Zn, favored superdeformed configurations are formed with two neutrons
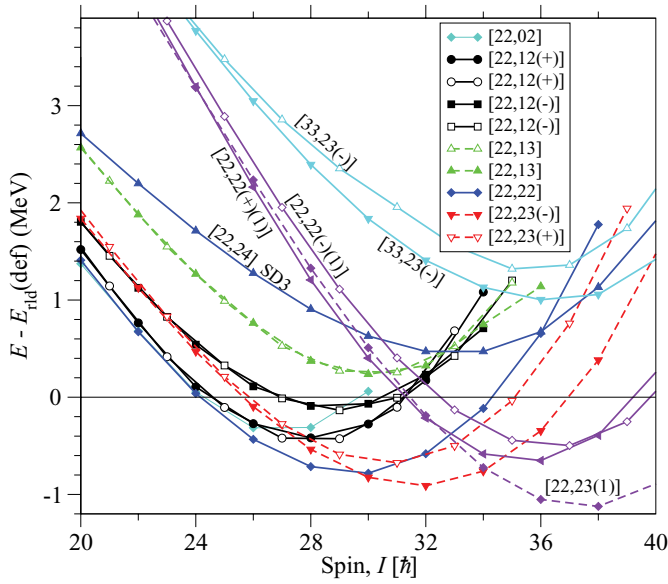
FIG. 29. (Color online) Same as Fig. 25 but for configurations associated with the superdeformed $Z = N = 30$ gap. Configurations with two neutrons in (fp), $1f_{7/2}$ and $1g_{9/2}$ orbitals above this gap are labeled in the legend, while labels are attached to the bands with one $h_{11/2}$ neutron (indicated by "(1)") and three proton holes in $1f_{7/2}$.

in these five orbitals. There are thus ten neutron configurations of this type which gives rise to the bands labeled in the legend of Fig. 29. At even higher spins, additional possibilities arise, for example, one neutron might be placed in the $\alpha = -1/2$ $1g_{9/2}$ orbital. Thus, if both neutrons above the $N = 30$ gap are placed in $1g_{9/2}$ orbitals, the [22,24] configuration is formed at a rather low energy (see Fig. 29). Another possibility is to place one neutron in the lowest $1h_{11/2}$ orbital, where three such bands which become yrast for $I \geqslant 35$ are shown in Fig. 29. A third possibility is to break the favored $Z = 30$ configuration and make a third proton hole in the $1f_{7/2}$ proton orbitals.

The calculated bands drawn in Fig. 29 are compared with the bands observed to spin values $I \approx 30$ and above, for positive parity in Fig. 30 and for negative parity in Fig. 31. Similar comparisons were presented in Ref. [18] but with some important additions in the present figures.[1] For positive parity the WD1 band which was also shown in Fig. 27 and assigned to the [22,02] configuration is included. The positive parity WD5 band has four $1g_{9/2}$ particles [Fig. 20(a)] and thus at least three $1f_{7/2}$ holes since it is observed beyond $I = 30$. The only low-lying odd-spin positive parity configurations in Fig. 29 are of the type [22,12] so band

---

[1]There is a small error in the moment of inertia calculation in Ref. [18], leading to an error roughly proportional to I^2 in the calculated energies with a maximum error of a few hundred keV for the highest spin values. Similarly, in Ref. [44] and subsequent publications, there is an error in the moment of inertia of the reference energy which is subtracted from the observed and calculated energies. Also this error amounts to a few hundred keV for the highest spin values in ^{62}Zn but it does not affect the differences between experiment and calculations. These errors do not change any conclusions about configuration assignments.
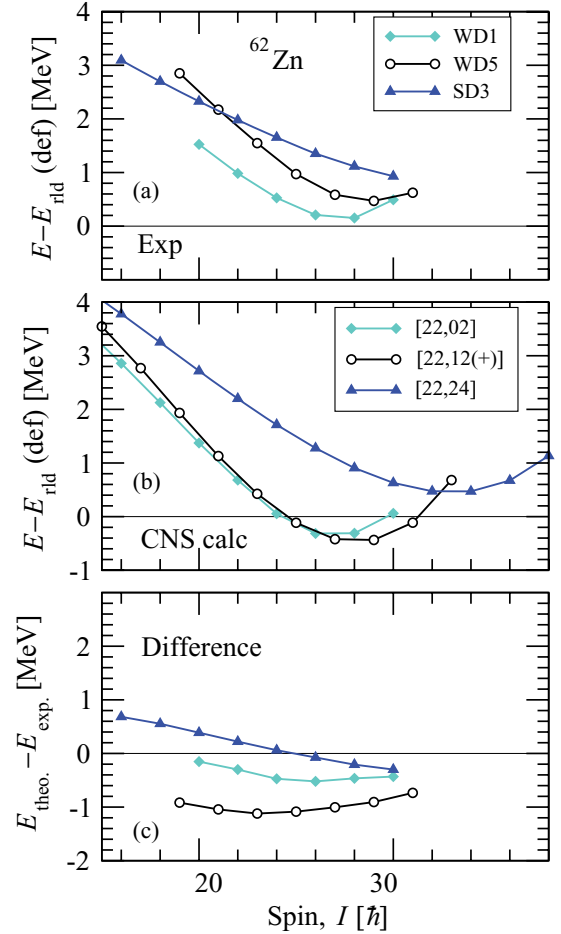

FIG. 30. (Color online) Same as Fig. 22 but for the superdeformed and strongly deformed bands with positive parity.

WD5 is assigned to the lowest-energy configuration of this type, [22,12(+)]. Furthermore, the SD3 band is assigned to the [22,24] configuration, as concluded previously in Ref. [18]. All these assignments appear to be rather well established considering the small and close to constant differences in the bottom panel of Fig. 29. However, it appears that the curvature of these difference curves are generally positive, corresponding to a larger curvature and thus a smaller $J^{(2)}$ in calculations compared with experiment. It was noticed in Ref. [55] that the $J^{(2)}$ moment of inertia is generally larger in the relativistic mean-field theory than in the CNS model. This suggests that it is energetically too expensive to build angular momentum in collective bands at large rotational frequencies in the modified oscillator model.

It was noticed in Sec. IV B that the WD4 and WD5 structures are very similar in the spin range where they are observed, $I = 19$–25. As there are two calculated odd-spin [22,12] bands with an energy differences similar to that of the WD4 and WD5 bands, it cannot be excluded that WD4 should be assigned to the lowest-energy band of this type, [22,12(+)] and WD5 to the higher-energy band, [22, 12(−)]. Puzzling pieces are the configurations that have not been observed: [22,22] which is calculated lowest in energy for $I \approx 30$, and
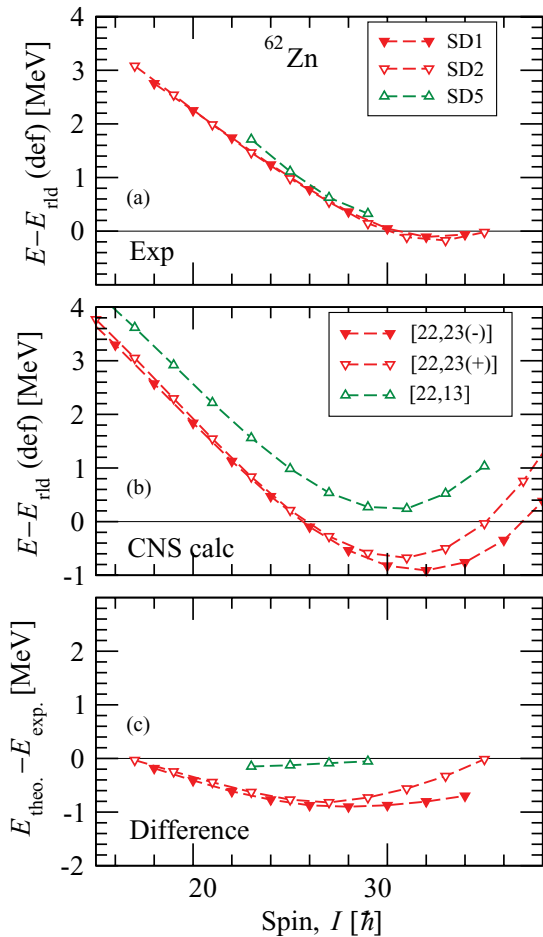
FIG. 31. (Color online) Same as Fig. 22 but for the superdeformed bands with negative parity.

the even spin signature partner of the odd spin [22,12(+)] configuration assigned to the WD5 band.

In the present level scheme, the negative-parity superdeformed band SD5 has been added compared with Ref. [18]. Thus, there are now three calculated bands which must be assigned to the two calculated signature partner configurations, [22,13] and [22,23], shown in Fig. 29. While the observed bands are at a very similar energy, the new SD5 band has a larger curvature, that is, a smaller value of $J^{(2)}$. This supports the conclusion in Ref. [18] that the SD1 and SD2 bands should be assigned to the [22,23] configuration with a higher spin content than the [22,13] configuration, which is thus assigned to the SD5 band. A problem with that interpretation is that the SD1 and SD2 bands are essentially signature degenerate which is a typical feature of the [22,13] bands with one neutron hole in the $1f_{7/2}$ orbitals but not for the [22,23] bands with an odd number of fp neutrons. However, the calculated [22,23] bands might very well become signature degenerate with a small change of the single-particle parameters. Note also that with the present assignment, a signature degenerate partner of SD5 can be expected.

The parity is not determined for the bands SD4 and WD9 and therefore they are more difficult to interpret. However, the SD4 band is interesting because it is comparatively low in en-

ergy at high spin and furthermore strongly downsloping when drawn relative to the rotating liquid drop reference. Indeed, the downslope is so steep that it is only the configurations in Fig. 29 with either a third $1f_{7/2}$ proton hole or with an $1h_{11/2}$ neutron which are reasonable candidates. Comparing calculations and experiment, the calculated downslope is too strong for the $\nu(h_{11/2})^1$ configurations and closer to experiment for the $\pi(1f_{7/2})^{-3}$ configurations. However, the latter are calculated more than 2 MeV above yrast. Therefore, it is not possible to give any conclusive interpretation of the SD4 band at present.

E. Calculated deformations

As discussed above, the different structures in ^{62}Zn are mainly characterized by the number of holes in the $1f_{7/2}$ orbitals q_1 and by the number of particles in $1g_{9/2}$ orbitals q_2. It was pointed out in Ref. [10] that the deformation at low spin values of the observed bands in ^{59}Cu is roughly proportional to $q = q_1 + q_2$ and this is true also for ^{62}Zn. For example, typical deformations are $\varepsilon_2 \approx 0.28$ for the configuration [11,02] ($q = 4$) assigned to TB2, $\varepsilon_2 \approx 0.33$ for the configuration [22,02] ($q = 6$) assigned to WD1, and $\varepsilon_2 \approx 0.40$ for the configuration [22,23] ($q = 9$) assigned to SD1, with γ values in the range $0°–30°$.

Structure ND9 ([01,02]) is a nice example of a favored termination with a well-localized minimum at $\gamma = 60°$. Adding just one hole in the $1f_{7/2}$ orbitals, this turns into the smoothly terminating band TB2 with a similar but softer minimum at $\gamma = 60°$. With one more hole in the $1f_{7/2}$ orbitals
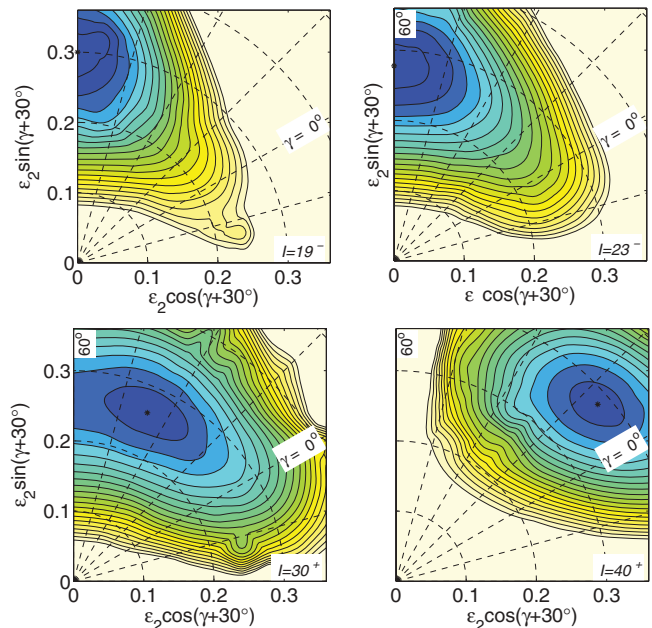

FIG. 32. (Color online) Potential energy surfaces illustrating the shape at termination for bands showing favored and unfavored terminations and nonterminating bands which remain collective at $I = I_{max}$. The potential energy surface at $I = I_{max}$ is shown for the [01(+),02], [11,02], [22,02], and [22,24] configurations assigned to the bands ND9, TB2a, WD1, and SD3. The contour line separation is 0.2 MeV with the "last" contour line 4 MeV above the minimum.

and one more $1g_{9/2}$ particle, WD1 is formed. This band appears to be an example of a nonterminating band [56] observed up to the I_{max} value, even though the lifetimes have not yet been measured. With the excitation of more particles and holes, the superdeformed bands are formed, which are not observed all the way to $I = I_{max}$ but where the calculated configurations are clearly strongly collective at that spin value (see Fig. 32).

It is also interesting to consider the value of the ε_2 deformation at $I = I_{max}$. Indeed, it turns out that at $\gamma = 60°$, holes in the low-lying $1f_{7/2}$ orbitals, which are downsloping with increasing oblate deformation, will rather counteract deformation. Thus, one would expect the absolute value of ε_2 to be roughly proportional to $q_2 - q_1$. This is illustrated in Fig. 32 where the oblate deformation at $I = I_{max}$ is larger for the [01,02] configuration than for the [11,02] configuration.

V. SUMMARY

The level scheme of ^{62}Zn is interesting in many aspects. First of all, it is one of the hitherto most comprehensive level schemes ever deduced. Second, it is a particularly illustrative example in the $A = 60$ region, simultaneously giving rise to features of both very light nuclei—where one nucleon makes decisive contributions to the structure of a specific configuration [57]—and heavy nuclei, namely by means of regular rotational bands. In the SD bands in the $A = 150$ region, for example, it is possible to follow the configurations with increasing particle number by adding one particle in a specific orbital [58,59]. This is quite similar to the possibility to follow the configurations in ^{62}Zn with subsequent excitations from the $1f_{7/2}$ shell into the fp orbitals and from the fp orbitals into the $1g_{9/2}$ shell as exemplified and summarized in Fig. 21. Indeed, the possibility to follow the configurations from close-to-spherical to large deformations from successive excitations of holes and particles appears unique to the $A \sim 60$ region [10,11,14].

Essentially all aspects of band termination [43] occur in ^{62}Zn. Thus, as exemplified in Fig. 32, structures ND9 and TB2 are nice examples of favored and unfavored band terminations while WD1 appears to correspond to a nonterminating band [56]. Finally, the SD bands are strongly collective at the highest spin values observed, which are two and three transitions short of I_{max} for SD2 and SD1, respectively, and they remain strongly collective also at $I = I_{max}$ according to the calculations.

A special feature of favored terminating states are that they might be fed by a large number of weak transitions as first pointed out for ^{157}Er [53]. This feature is seen for several states in ^{62}Zn, in particular the 16^+ state of structure ND6, the 17^+ state of structure ND7, or the 19^- state of structure ND9. For example, more than 20 transitions feeding the ND6 16^+ state are observed in ^{62}Zn. Hitherto, a comparable resolution could only been presented for the decay-out regime of the yrast superdeformed band in ^{59}Cu [13].

The comparison between calculations and experiment gives suggestions on how the single-particle parameters might be modified to improve the theoretical description. In line with comparable extensive studies for other nuclei in the region, it appears that the gap for particle number 28 should rather be somewhat enlarged while the energy cost to excite particles to the $1g_{9/2}$ shell should be slightly decreased. Furthermore, the relative low-lying highest-spin states of structures ND3 (14^-) and ND7 (17^+) in ^{62}Zn suggest that the spacing between the $2p_{3/2}$ and $1f_{5/2}$ shells should be reduced. Such investigations require and deserve a separate study.

[1] I.-Y. Lee, Nucl. Phys. A **520**, 641c (1990).
[2] D. G. Sarantites *et al.*, Nucl. Instrum. Methods Phys. Res., Sect. A **381**, 418 (1996).
[3] D. Rudolph *et al.*, Phys. Rev. Lett. **80**, 3018 (1998).
[4] D. Rudolph, C. Baktash, M. Devlin, D. R. LaFosse, L. L. Riedinger, D. G. Sarantites, and C. H. Yu, Phys. Rev. Lett. **86**, 1450 (2001).
[5] D. Rudolph *et al.*, Phys. Rev. Lett. **82**, 3763 (1999).
[6] E. K. Johansson *et al.*, Phys. Rev. C **77**, 064316 (2008).
[7] C.-H. Yu *et al.*, Phys. Rev. C **60**, 031305(R) (1999).
[8] W. Satula, J. Dobaczewski, W. Nazarewicz, and M. Rafalski, Phys. Rev. C **81**, 054310 (2010).
[9] D. Rudolph *et al.*, Phys. Rev. Lett. **96**, 092501 (2006).
[10] C. Andreoiu *et al.*, Eur. Phys. J. A **14**, 317 (2002).
[11] E. K. Johansson *et al.*, Phys. Rev. C **80**, 014321 (2009).
[12] D. Rudolph *et al.*, J. Phys. G **37**, 075105 (2010).
[13] C. Andreoiu *et al.*, Phys. Rev. Lett. **91**, 232502 (2003).
[14] L.-L. Andersson *et al.*, Eur. Phys. J. A **36**, 251 (2008).
[15] C. E. Svensson *et al.*, Phys. Rev. Lett. **82**, 3400 (1999).
[16] L.-L. Andersson *et al.*, Phys. Rev. C **79**, 024312 (2009).

[17] C. E. Svensson *et al.*, Phys. Rev. Lett. **79**, 1233 (1997).
[18] J. Gellanki *et al.*, Phys. Rev. C **80**, 051304(R) (2009).
[19] J. Ekman *et al.*, Phys. Rev. C **66**, 051301(R) (2002).
[20] C. E. Svensson *et al.*, Phys. Rev. Lett. **80**, 2558 (1998).
[21] A. Galindo-Uribarri *et al.*, Phys. Lett. B **422**, 45 (1998).
[22] W. Reviol *et al.*, Phys. Rev. C **65**, 034309 (2002).
[23] D. A. Torres *et al.*, Phys. Rev. C **78**, 054318 (2008).
[24] D. Karlgren *et al.*, Phys. Rev. C **69**, 034330 (2004).
[25] C. Andreoiu *et al.*, Phys. Rev. C **62**, 051301(R) (2000).
[26] D. Rudolph *et al.*, Eur. Phys. J. A **14**, 137 (2002).
[27] M. Devlin *et al.*, Nucl. Instrum. Methods Phys. Res., Sect. A **383**, 506 (1996).
[28] C. E. Svensson *et al.*, Nucl. Instrum. Methods Phys. Res., Sect. A **396**, 288 (1997).
[29] See Supplemental Material at http://link.aps.org/supplemental/10.1103/PhysRevC.86.034304 for a detailed version of the excitation scheme of ^{62}Zn.
[30] D. Seweryniak *et al.*, Nucl. Instrum. Methods Phys. Res., Sect. A **340**, 353 (1994).
[31] D. C. Radford, Nucl. Instrum. Methods Phys. Res., Sect. A **361**, 297 (1995).

[32] J. Theuerkauf, S. Esser, S. Krink, M. Luig, N. Nicolay, O. Stuch, and H. Wolters, Program Tv, University of Cologne (unpublished).

[33] K. S. Krane, R. M. Steffen, and R. M. Wheeler, At. Data Nucl. Data Tables **11**, 351 (1973).

[34] M. K. Kabadiyski, K. P. Lieb, and D. Rudolph, Nucl. Phys. A **563**, 301 (1993).

[35] D. Rudolph *et al.*, Eur. Phys. J. A **4**, 115 (1999).

[36] H. J. Rose and D. M. Brink, Rev. Mod. Phys. **39**, 306 (1967).

[37] J. F. Bruandet, Tsan Ung Chan, M. Agard, J. P. Longequeue, C. Morand, and A. Giorni, Z. Phys. A **279**, 69 (1976).

[38] L. Mulligan, R. W. Zurmühle, and D. P. Balamuth, Phys. Rev. C **19**, 1295 (1979).

[39] N. J. Ward, L. P. Ekström, G. D. Jones, F. Kearns, T. P. Morrison, O. M. Mustaffa, D. N. Simister, P. J. Twin, and R. Wadsworth, J. Phys. G **7**, 815 (1981).

[40] K. Furutaka *et al.*, Z. Phys. A **358**, 279 (1997).

[41] J. Gellanki, Licentiate thesis, Lund University, LUNFD6(NFFR-3112)/1-73/(2011).

[42] T. Bengtsson and I. Ragnarsson, Nucl. Phys. A **436**, 14 (1985).

[43] A. V. Afanasjev, D. B. Fossan, G. J. Lane, and I. Ragnarsson, Phys. Rep. **322**, 1 (1999).

[44] B. G. Carlsson and I. Ragnarsson, Phys. Rev. C **74**, 011302(R) (2006).

[45] S. G. Nilsson and I. Ragnarsson, *Shapes and Shells in Nuclear Structure* (Cambridge University Press, 1995).

[46] S. G. Rohoziński and A. Sobiczewski, Acta Phys. Pol. B **12**, 1001 (1981).

[47] V. M. Strutinsky, Nucl. Phys. A **95**, 420 (1967).

[48] G. Andersson *et al.*, Nucl. Phys. A **268**, 205 (1976).

[49] K. Pomorski and J. Dudek, Phys. Rev. C **67**, 044316 (2003).

[50] K. T. R. Davies and J. R. Nix, Phys. Rev. C **14**, 1977 (1976).

[51] A. L. Goodman, Nucl. Phys. A **230**, 466 (1974).

[52] I. Ragnarsson, V. P. Janzen, D. B. Fossan, N. C. Schmeing, and R. Wadsworth, Phys. Rev. Lett. **74**, 3935 (1995).

[53] A. O. Evans *et al.*, Phys. Rev. Lett. **92**, 252502 (2004).

[54] C.-H. Yu *et al.*, Phys. Rev. C **62**, 041301(R) (2000).

[55] A. V. Afanasjev, I. Ragnarsson, and P. Ring, Phys. Rev. C **59**, 3166 (1999).

[56] J. J. Valiente-Dobón *et al.*, Phys. Rev. Lett. **95**, 232501 (2005).

[57] I. Ragnarsson, S. Åberg, and R. K. Sheline, Phys. Scr. **24**, 215 (1981).

[58] I. Ragnarsson, Nucl. Phys. A **557**, 167c (1993).

[59] W. Nazarewicz and I. Ragnarsson, *Handbook of Nuclear Properties*, edited by D. N. Poenaru and W. Greiner (Clarendon Press, Oxford, 1996), p. 80.